POLITECNICO DI TORINO

Master's Degree in Aerospace Engineering

Master's Thesis

Numerical analysis of the mixing losses in a 1.5 stage turbine

Supervisors

Prof. Nicolas BINDER

Prof. Roberto MARSILIO

Prof. Luigi VIGEVANO

Candidate

Greta RAINA

December 2021

Abstract

As the aviation industry is experiencing a rapid growth, the need to reduce aircraft fuel consumption is becoming more and more urgent, both for economic and environmental reasons. As turbines are the engine components with the strongest impact on consumption, it is important to acknowledge what losses characterize turbine flows and how they can be minimized, in order to improve turbine design and reduce CO_2 emissions. This work aims at strengthening understanding of the losses generated by wakes mixing in downstream rows. The wake decay rate is mainly due to two mechanisms: viscous mixing, which results in loss, and a reversible process that varies the depth of the wakes. Contradictory information is still present in literature on whether the latter phenomenon coincides with a wake depth increase or reduction. To answer this question, a comparison between a co-rotating and a counter-rotating 1.5 stage axial turbine is carried out by means of numerical simulations: it emerges that rotor wakes are dilated as they pass through a downstream vane row belonging to a co-rotating turbine configuration, while they are stretched if the vane is part of a counter-rotating stage. The size of the wakes is reduced as they undergo stretching - leading to smaller overall losses than if viscosity was acting alone to mix out the wakes -, while the opposite occurs in the case of wake dilation. Therefore, it is found that employing a counter-rotating turbine configuration allows to contain losses associated to wake-mixing in turbines.

Table of Contents

List of Tables

List of Figures

Nomenclature

Acronyms

BPP	Blade Passing Period
BPF	Blade Passing Frequency
CRT	Counter-Rotating Turbine
HP	High Pressure
LP	Low Pressure
MP	Mixing Plane
R	Rotor
RMS	Root Mean Square
SM	Sliding Mesh
TVF	Turbine Vane Frame
V	Vane
WVR	Wake Velocity Ratio

Latin letters

c	Blade chord length
C	Contour for circulation calculation
Cp	Isobaric specific heat
H	Stagnation enthalpy
p	Pressure

r	Radius
s	Entropy
T	Temperature
u	Axial velocity
U	Free-stream velocity
V	Velocity magnitude
W	Relative velocity
x	Axial direction

Greek letters

α	Absolute flow angle
β	Relative wake depth
η	Efficiency
ξ	Total pressure loss coefficient
ρ	Density
ω	Rotational speed

Symbols & Indices

$(\cdot)_{co}$	Referred to the co-rotating turbine
$(\cdot)_{counter}$	Referred to the counter-rotating turbine
$(\cdot)_i$	i chords downstream
$(\cdot)_{in}$	Domain inlet
$(\cdot)_{is}$	Isentropic
$(\cdot)_{MO}$	Mixed-out quantity
$(\cdot)_{out}$	Domain outlet
$(\cdot)_t$	Total (stagnation) conditions
$\hat{(\cdot)}$	Normalized quantity

Chapter 1

Introduction

As the aviation industry is growing fast, the need to reduce aircraft fuel consumption and noise levels is becoming more and more urgent, both for economic and environmental reasons. This can be achieved through various measures, which concern the design of the aircraft and of the engines. Regarding the latter, nowadays the tendency is to increase the by-pass ratio of civil turbofan engines in order to reach higher propulsive efficiencies. This allows to reduce specific fuel consumption, thus lowering CO_2 emissions. However, it leads to larger fan diameters, which impose some limitations on the revolution speed of the low-pressure shaft, in order to avoid excessive Mach number values at the blade tip. This also has an impact on the turbine architecture: to maintain a reasonable circumferential speed, the low-pressure turbine is subject to an increase in the mean radius, therefore running on much larger diameters than the high-pressure turbine. At the same time, in order to limit the axial length of the engine and therefore its weight, the two turbines should be placed as closed as possible. Such constraints concerning the axial and radial dimensions of the engine pose some problems in the modelling of the inter-turbine duct, or mid turbine frame, meaning the channel which connects the two turbines (figure 1.1). Indeed, the duct has to be designed short and steep, being therefore characterized by a pronounced curvature and an area increase which leads to adverse pressure gradients [1]. The evolution of the low-pressure turbine architecture is summarized in figure 1.2.

The inter-turbine duct is characterized by the presence of structural and service devices, which cross the channel and are enveloped in fairings in order to minimize the aerodynamic impact. In some modern cases, such as the Pratt & Whitney PW1000G engine, these fairings are cambered: in this way, they can provide a certain deviation to the flow. This

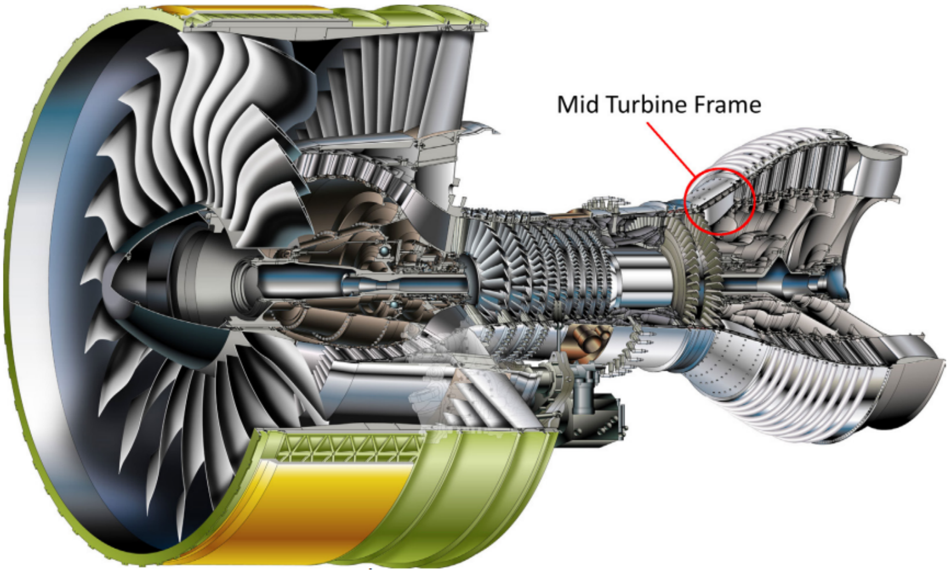

Figure 1.1: Engine Alliance GP7200: example of mid turbine frame.

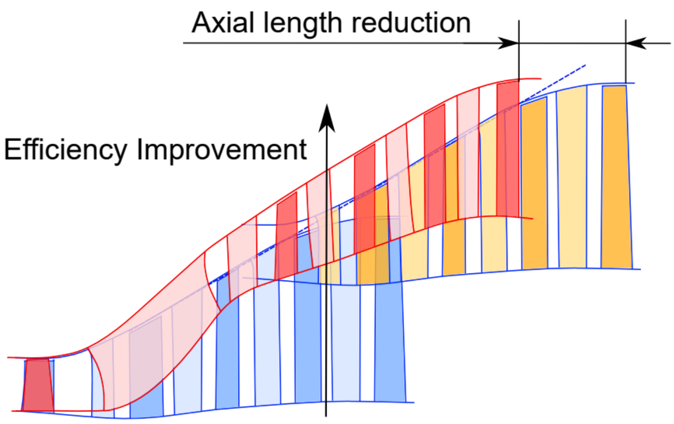

Figure 1.2: Blue: LP turbine of a conventional turbofan. Orange: increased mean radius due to higher bypass ratios. Red: modern configuration with reduced axial length. [2]

solution, which takes the name of Turbine Vane Frame (TVF), allows to remove the first low-pressure vane row, reducing parts count and cutting down on weight. However, these fairings are characterized by a very low aspect ratio, resulting in enhanced secondary flows, which can strongly impact performances. Moreover, the flow passing through the duct is extremely uneven, as it has been polluted by the tip-gap vortices, wake patterns and cooling flows incoming from the upstream high-pressure turbine [2]. Such distortions lead to higher losses as they convect in an environment subject to adverse pressure gradients [3], like the one that characterizes the TVF. To contain entropy production, it is therefore essential to understand how to properly model this channel: this is especially important since turbines are the engine components with the strongest impact on consumption[1]. Unfortunately, most of the loss mechanisms above cited are not yet fully understood, which makes it difficult to evaluate the significance of such losses and bring about improvements.

This issue is being addressed by the French aerospace engine manufacturer Safran Aircraft Engines, through a PhD project conducted in conjunction with the Aerodynamics, Energetics and Propulsion Department (DAEP) of the ISAE-SUPAERO (*Institut Supérieur de l'Aéronautique et de l'Espace*) in Toulouse, France. In this context, the present work represents the outcome of a six-month internship completed in the DAEP department in support of such PhD project. The aim is to improve the design of the turbine vane frame by strengthening understanding of one of these loss mechanisms characterizing turbine flows: the mixing of wakes as they convect in the downstream row. This study allows to isolate the phenomenon of the wake-mixing losses and shed light on the mechanisms behind it, on which there is still a lack of consensus in the literature. The analysis is carried out by means of URANS-based numerical simulations on various turbine configurations, with the purpose of comparing two general cases:

- a common dual-spool turbine, in which the high-pressure and low-pressure shafts rotate in the same direction;
- a less used dual-spool turbine with counter-rotating shafts.

Comparison between these two cases allows to explore how the wakes generated by the HP rotor evolve in the downstream LP vane - which in the presence of a TVF coincides with the cambered fairings - and the amount of losses generated.

The work is organised as follows: chapter 2 provides an overview of the state of the art of the analysis of the wake-mixing losses, as well as of counter-rotating turbines. This chapter introduces the notions necessary to the comprehension of the subject and highlights the relevance and the originality of the present study. Chapter 3 illustrates and motivates the choices made in the selection of the turbine setup. It is divided in two sections: in the first, the turbine architecture is described, along with the adjustments that were made in order to make it suitable for this analysis. The second section deals with the numerical aspects: it is split in three short subsections, detailing the creation of the mesh, the numerical

[1]A gain of 1% in the turbine polytropic efficiency results in a gain of 0.96% in specific fuel consumption. For the fan, a gain of 1% in polytropic efficiency results in a gain of 0.62% in specific fuel consumption. For the high-pressure and low-pressure compressors, the gain is respectively 0.22% and 0.66% [4].

schemes and models employed, and the boundary and initial conditions applied to each configuration. In chapter 4 the outcomes of this work are described: the first two sections present the results obtained with the two configurations delineated in the last part of the previous chapter, while the third section introduces a subsequent analysis that was carried out in order to further investigate the subject. Finally, in chapter 5 conclusions are drawn and future work is suggested.

Chapter 2

Wake-mixing losses

This chapter introduces the notions which are necessary to understand the following parts of this work and illustrates the context in which the study has been carried out. The first section gives some background about fluid wakes and their decay process, with a focus on the influence of pressure gradients. The second section explains how these concepts find application in turbomachinery: firstly, the mechanism of wake-mixing in compressors is briefly described. Secondly, the diverging opinions regarding the effects of the downstream row on wake decay in turbines are presented. This overview of the state of the art of the phenomenon will allow to justify the utility of the present work at the end of the chapter.

2.1 Effects of pressure gradients on wake decay

A wake can be defined as the region of disturbed flow downstream of a solid body surrounded by or moving through a fluid. The wake velocity profile is shown in figure 2.1, where U is the free-stream velocity, u_c is the velocity at the wake centerline and β is the relative wake depth, defined as:

$$\beta = \frac{U - u_c}{U}. \tag{2.1}$$

Always in figure 2.1, b and δ are different parameters that represent the wake width.

The decay of wakes in constant-pressure flows has been thoroughly studied by several authors, including Schlichting [6]. When considering the flow around a profile in a duct of constant cross-sectional area, as the wake evolves downstream of it, β will pass from 1 -

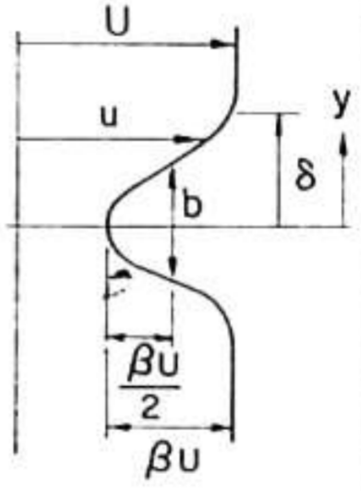

Figure 2.1: Parameters describing the wake velocity profile. [5]

meaning that u_c is zero, at the profile trailing edge - to 0 - when u_c has reached the same value as the free-stream velocity and the wake has mixed out completely.

Hill et al. [5] were the first to investigate how the presence of pressure gradients can influence wake decay. Hill analysed the evolution of the wake generated by an aluminium bar in a diffusing section with variable divergence angle. Measuring the velocity profile at different stations along the diffuser, he demonstrated experimentally that the wake depth decreases less rapidly when the flow is subject to adverse pressure gradients (figure 2.2). Thus, the wake decay process is slowed down with respect to the constant-area case.

For an inviscid fluid in a diffuser, the velocity gap between the wake and the free-stream even grows. This is shown by the differential momentum equation:

$$\frac{du}{dx} = -\frac{1}{\rho u}\frac{dp}{dx}. \tag{2.2}$$

A slower fluid, here the wake, is more affected by a given pressure gradient than a faster one, that is the free stream. Thus, in the case of favourable pressure gradients ($\frac{dp}{dx} < 0$) the wake undergoes a stronger acceleration than the free-stream, while in the presence of adverse pressure gradients ($\frac{dp}{dx} > 0$) the wake slows down more than the surrounding fluid, meaning that the relative wake depth increases. For a viscous fluid, diffusion tends to counteract the pressure force, delaying the wake depth increase.

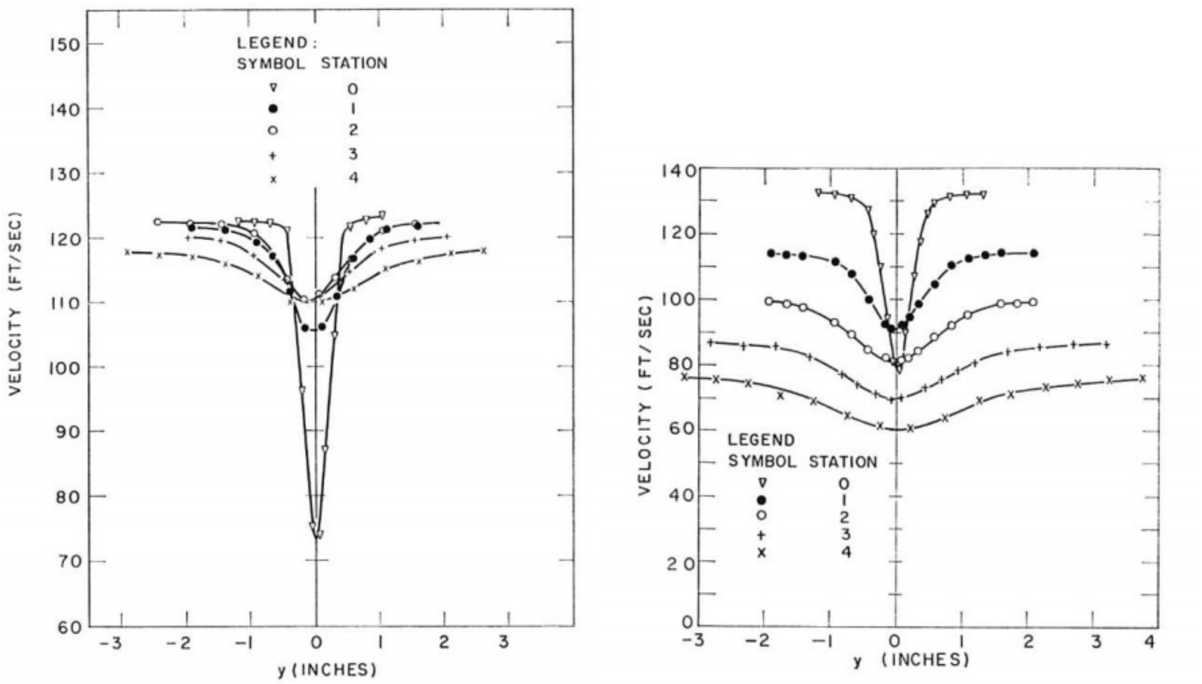

(a) Nearly constant pressure. (b) Positive axial pressure gradient.

Figure 2.2: Wake velocity profile measured at five stations downstream of an aluminum bar. [5]

2.2 Wake-mixing in turbomachinery: loss variations due to downstream rows

The study of Hill et al. [5] on the effects of a diffuser on wake decay is relevant to the field of turbomachinery. Following his work, Smith introduced the concept of "wake recovery" [7] to describe how wakes in axial compressors are stretched, or contracted, through a reversible process, as they enter the downstream row. Such contraction is beneficial as it causes an inviscid reduction of the wake velocity gap, therefore attenuating the wake-mixing losses compared to the constant-area case. The effects of wake recovery in compressors were then experimentally demonstrated by Van Zante et al. [8], who also developed a model to evaluate the relative contributions of inviscid stretching and viscous dissipation to the wake decay, predicting that the former mechanism is dominant.

While there is consensus that the wake-mixing losses are attenuated in compressors thanks to the stretching of wake fluid streams, contradictory views are still present in the open literature concerning the effect of downstream rows on wake decay in turbines.

Experimental evidence of this relatively weak unsteady phenomenon is limited: Hodson and Dawes [9] and van de Wall et al. [10] provided a contribution in this regard. Hodson and Dawes [9] measured the mixing losses as the wakes convect through the adjcent row of a turbine cascade and reported an increase by a factor of two compared to the constant-area mixing. Van de Wall et al. [10] developed a transport model able to take the recovery process into account and validated it against experimental results: according to their study, the interaction of the wake with the downstream blade row results in a significant increase in the wake-mixing losses. The work of Praisner et al. [11] is in line with these results, as it demonstrates that "*wakes in turbines are dilated in the adjacent downstream row*" [11], be it a vane or a blade row. According to Praisner, the phenomenon of the wake-mixing losses should be analysed in the wake-generation reference frame.

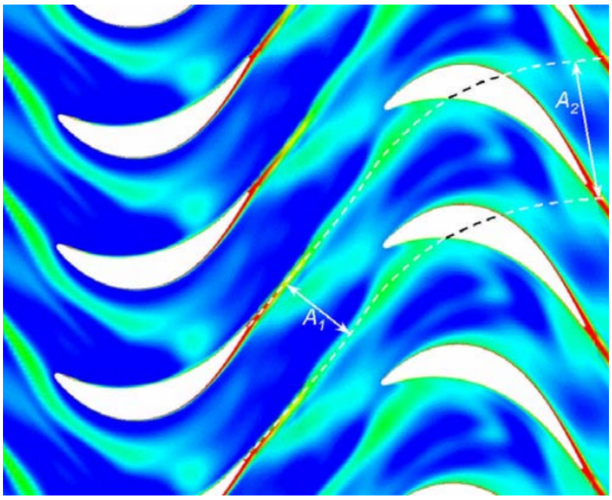

Figure 2.3: Instantaneous entropy distributions with time-mean wake paths from a time-accurate simulation of an LPT. [11]

Figure 2.3 highlights the inviscid stream-tube dilation occurring as the wakes convect through the downstream row. Praisner introduces the Wake Velocity Ratio:

$$WVR = \frac{V_2}{V_1}, \tag{2.3}$$

where V_1 and V_2 represent respectively the inlet and outlet free-stream velocities related to the segment over which the area change takes place (e.g. between sections A_1 and A_2 in figure). The velocity variation is expressed in the wake-generation reference frame, instead of the reference frame of the local airfoil row. As the area is shown to increase, the WVR will be less than unity across turbine blades, while the opposite occurs in compressors. Praisner has also quantified the mixing losses variation as a function of such velocity ratio, concluding that the loss increase due to wake dilation is more important than the loss reduction associated to wake stretching. Indeed, the former phenomenon can cause an efficiency loss of up to 1.5% in LP turbines [11], where wake-mixing losses can be increased by more than 100% above the constant-area (WVR = 1.0) level. This is plotted in figure 2.4, in which losses are defined as follows:

$$\xi = \frac{(p_{t1} - p_{t2_{MO}})}{p_{t1}} \cdot 100, \tag{2.4}$$

where p_t is the mass averaged total pressure and MO indicates a mixed-out quantity.

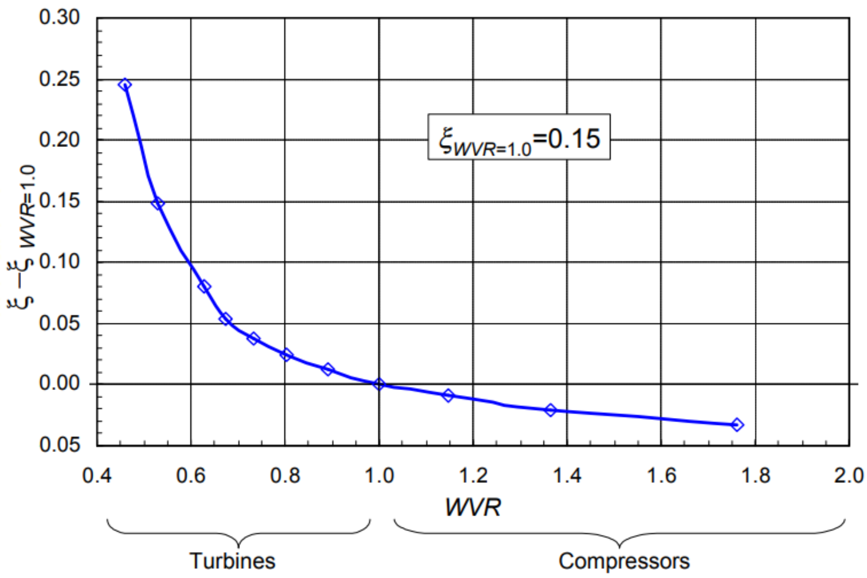

Figure 2.4: Modification of wake-mixing losses in turbomachines with respect to the constant-area case, as a function of the Wake Velocity Ratio. [11]

All the studies introduced so far support the hypothesis that wake-mixing losses are increased in turbines as the wake passes through the downstream row. This suggests that, if it was possible to adopt a different stage configuration able to accelerate the flow in the wake-generation reference frame, wake-mixing losses in turbines could be significantly reduced, just like in compressors.

However, studies from Rose and Harvey [12], followed by those of Rose et al. [13] and Marx et al. [14], introduce an opposite view, according to which wake losses are attenuated in turbines. The authors state that it is not sufficient to evaluate whether the flow is accelerated or diffused in the downstream row, as "*acceleration is a zero work, isentropic, adiabatic process*" [12], while turbines are machines in which high work exchange is involved.

As first stated by Dean [15], the only isentropic way to exchange enthalpy with a flowing fluid is unsteadily. When considering equation 2.5, which is the energy equation for a compressible, inviscid, adiabatic flow field, it is well known that both terms are negative for turbines. This means that the more time the fluid spends between the rotor blades, the more enthalpy is extracted from it: this concept is referred to as "differential work" [12].

$$\frac{DH}{Dt} = \frac{1}{\rho} \frac{dp}{dt} \tag{2.5}$$

Smith [16] had relied on the hypothesis that the wake is slower than the fluid - and therefore takes longer to pass through the rotor blades - concluding that wake losses are increased. Instead, Rose et al. [13] carried out a Lagrangian study that led to the opposite conclusion: as shown in figure 2.5, the wake particles passing through the rotor are subject to higher acceleration than the surrounding flow. The author attributes this phenomenon to the so-called "negative jet effect", meaning that the wake fluid migrates toward the suction side of the blade, where the pressure is lower, while the free-stream moves to the pressure side of the passage. This results in a reduction of the wake entropy and therefore of the turbine wake-mixing losses. In this scenario, stronger unsteady interaction could further reduce mixing losses - although problems linked to noise and flow separation would arise.

It emerges that the phenomenon of the mixing-losses in turbines needs to be further explored, as the effects of the downstream row on wake decay are not clear. On the one hand, some scholars state that losses are increased as the wakes convect through the adjacent turbine blades. On the other hand, some authors support the hypothesis that losses are reduced in turbines just as in compressors. It is important to better understand this phenomenon, since only by knowing the origin and the nature of the losses will it be possible to quantify them and reduce them, improving turbines design and performance.

The present work aims at investigating whether it is true that flow acceleration in the wake-generation reference frame leads to a reduction in the wake-mixing losses occurring in turbines. To do so, a standard 1.5 turbine stage configuration - consisting of one HP stage followed by a LP vane - will be compared to a counter-rotating configuration, obtained by retaining the design of the HP stage and redesigning the LP vane. As the vane belonging to a counter-rotating LP stage causes the flow leaving the rotor to accelerate in the rotating reference frame, this study will allow to analyse the mechanisms of loss and recovery more in depth.

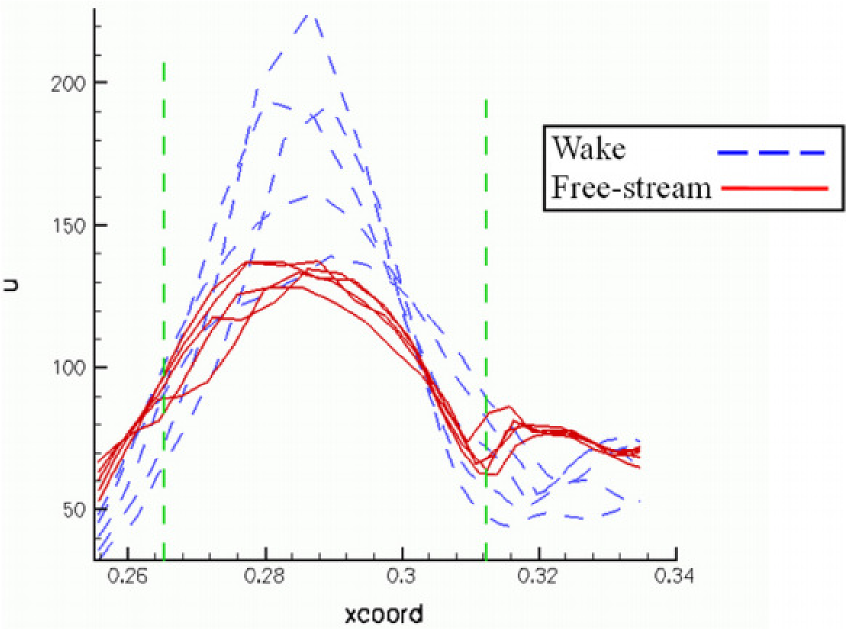

Figure 2.5: Lagrangian output processing for free-stream and wake particles passing through the rotor. The green lines represent the leading edge and trailing edge of the rotor. u is the axial velocity in m/s. [13]

At present, only few working counter-rotating engines exist, and they consist of small-sized motors - e.g. RB211, EJ200, F119-PW-100. Nevertheless, the development of counter-rotating turbines has gained more interest in recent years. Indeed, counter-rotating turbines (CRTs) have already been investigated by several authors and it is known that they can offer superior performances over the conventional co-rotating configurations. Some of the advantages of adopting a CRT are detailed by Louis [17] and Rajeevalochanam et al. [18].

A vaneless CRT stage consists of two adjacent rows with dissimilar bladings rotating at the same velocity in opposite directions. Stationary vanes are absent: the efficiency improvement in vaneless CRTs is therefore primarily linked to the elimination of the vanes, which leads to a reduction in the engine's weight and axial length. Instead, in vaned CRT dual-spool engines, the two spools rotate in opposite directions and the LP turbine is referred to as vaned CRT. In this case, efficiency improvements are of the order of 2% at design point [18]. This is mainly due to the reduced deflection of the flow in the vane row - around 30° instead of 90° as in the co-rotating case - which coincides with smaller profile and secondary losses. However, the consequences of employing counter-rotating turbines on wake decay have not yet been investigated. The novelty of the present work lies in the fact that it evaluates the losses generated as HP rotor wakes mix in the downstream LP vane, comparing a co-rotating LP turbine with a vaned counter-rotating one. This has never been done before and it will allow to estimate the impact of the mixing-losses as the flow is stretched or dilated in the wake-generation reference frame and to assess a further advantage of adopting CRTs. This is especially important in view of improving the design of the fairings of the TVF, by minimizing entropy production associated to this particular loss mechanism.

Chapter 3

Geometry and numerics

This study is carried out by means of numerical simulations, using the elsA CFD software, developed by ONERA for turbomachinery and external aerodynamics applications. As mentioned in the previous chapter, the scope of this work is to analyse the behaviour of rotor-generated wakes as the flow passes through the downstream vane row, with the purpose of ameliorating the design of the TVF. This is done by investigating whether a counter-rotating design, by accelerating the flow in the rotating frame, allows to set off a recovery mechanism, thus reducing the losses associated to wake decay. In order to isolate the phenomenon of wake-mixing, the study does not employ a real TVF configuration, in which the flow would be subject to various types of disturbances, some of which having a stronger impact than the investigated mechanism. Instead, the selected configuration is a very simple and academic one. In the following sections, it is described both from a geometrical and numerical point of view.

3.1 The selected configuration

The turbine architecture selected for this study is the Aachen 1.5 stage turbine rig, whose characteristics are detailed in figure 3.1 and table 3.1. The Aachen turbine is a cold air turbine owned by the Institute of Jet Propulsion and Turbomachinery of the RWTH Aachen University, in Germany. It has a simple geometry, with a constant mean radius and hub-to-tip ratio. The blades of the three rows are untwisted and the two stationary vanes are identical. The special feature of this turbine, which led to its selection for the present work, is the fact that the absolute velocity of the flow at the exit of the rotor is aligned with the axial direction: this allows comparison of the standard configuration

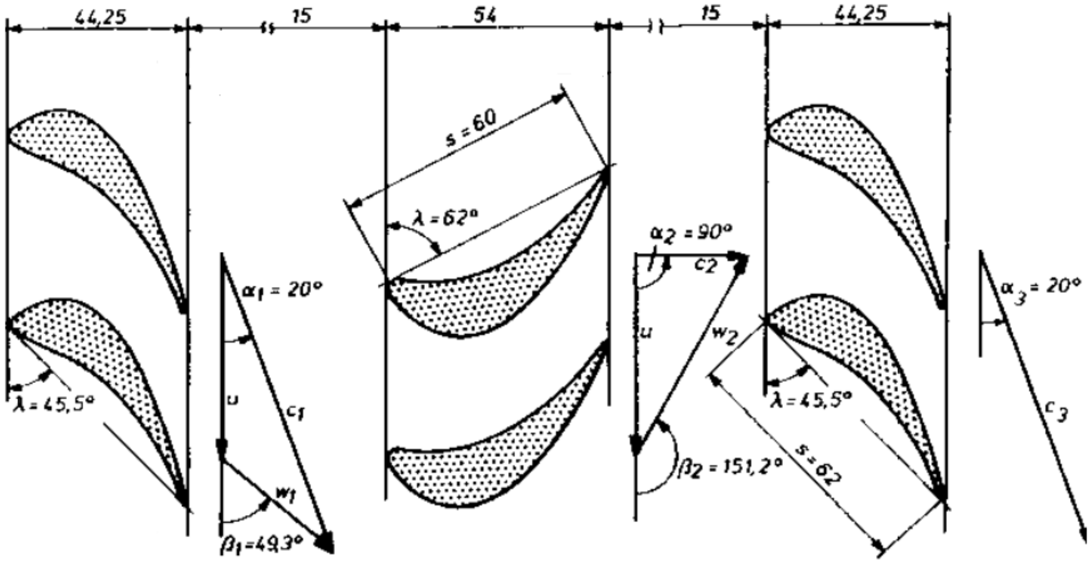

Figure 3.1: Blade profiles and velocity triangles of the Aachen 1.5 stage axial turbine. [19]

	Vanes	*Rotor*
Blade number	36	41
Rotational speed [rpm]	–	3500
Tip radius [mm]	300	300
Pitch (midspan) [mm]	47.6	41.8
Channel height [mm]	55.0	55.0

Table 3.1: Characteristics of the Aachen turbine.

(represented in figure 3.1) with a new one in which the last row is symmetrically reoriented, so to establish a counter-rotating turbine configuration. The first two rows of the Aachen turbine can thus be seen as a HP turbine stage, while the third row coincides with the first LP vane and plays the role of a TVF. This last row belongs to a co-rotating stage in one case and to a counter-rotating one in the other.

Comparing the losses strictly connected to wake-mixing without biasing the results is not straightforward. Firstly, as described in chapter 2, the difference in flow deflection leads to a performance gap between a co-rotating and a vaned counter-rotating turbine: as the deviation angle is lower in CRTs, the losses associated to the boundary layer and to secondary flows are reduced. Another factor influencing performance is the flow angle of attack: when the flow reaches the leading edge of the downstream row blades with an under-incidence, this results in a more favourable condition than when it arrives with an over-incidence. Therefore, in order to eliminate such differences in performance, the two tested configurations have to respect the following requirements:

- the same deflection should be given to the flow by the LP vane in the co-rotating and in the counter-rotating case;
- the flow incidence at the LP vane leading edge should be the same in the two cases.

The first point explicates why in this study the counter-rotating case is realized by mirroring the LP vane with respect to the meridional plane, preserving the same blade geometry. The second point justifies the choice of employing the Aachen turbine geometry, which is designed so that the flow leaving the first stage is axial.

Figure 3.2 schematically depicts the velocity triangles in the co-rotating and counter-rotating case. For simplicity, only the HP rotor and the two different LP vanes are shown. It can be seen that the absolute and tangential velocity of the flow leaving the vane are instead identical for the two solutions. Instead, regarding the relative velocity, in the co-rotating case W_3 is smaller than W_2, while in the counter-rotating case W_3' is bigger than W_2. Hence, in the two cases the flow undergoes respectively deceleration and acceleration in the rotor reference frame (as also shown in figure 3.3), meaning that stream-tubes are respectively dilated and stretched. The comparison between the two will therefore allow to understand the mechanisms of loss and recovery more in depth.

Despite the apparent symmetry of the two compared geometries, there is still one source of asymmetry that could pollute the analysis. Since the blades of the Aachen turbine are untwisted and the hub-to-tip ratio is not close to unity, the angle of incidence of the flow at the exit of the rotor varies significantly between the hub and the tip of the blade. Indeed, the tangential velocity is expressed as $\omega \cdot r$, where ω is the revolution speed and r is the local radius. As ω is constant, the tangential velocity increases with the radius. Since the direction of W_2 remains unchanged, the absolute velocity profile is characterized by a non-zero incidence above and below the mean radius (figure 3.4).

This affects the span-wise symmetry of the flow entering the two vanes and could therefore bias the comparison. To avoid such asymmetry, the mean radius of the Aachen turbine was extended by 210 times, so to guarantee that $\Delta\alpha_{hub-tip} < 0.1°$. The blade size and geometry were preserved and the rotational speed was adapted in order to keep the velocity triangles - and therefore the load coefficient - unchanged. The Mach and Reynolds numbers also

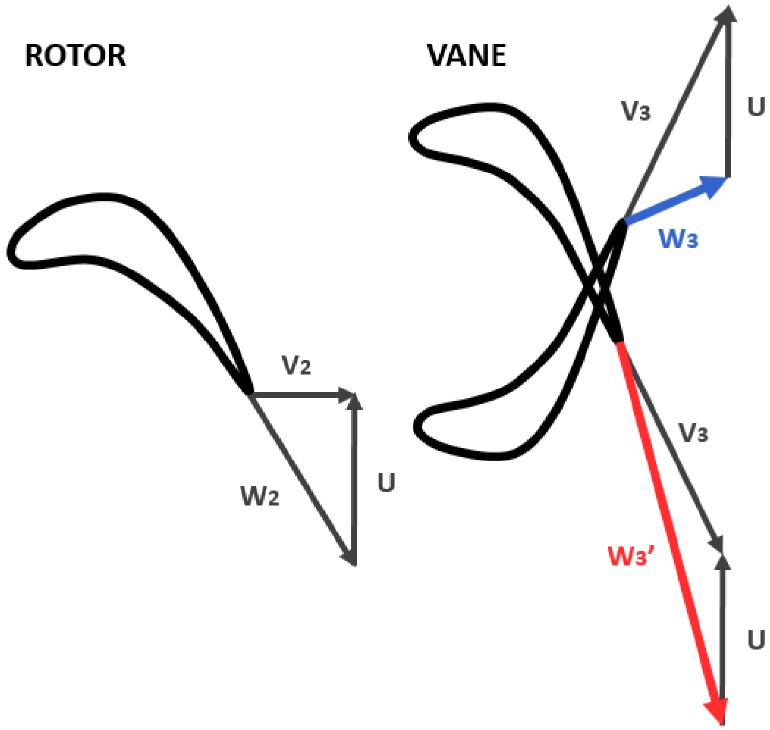

Figure 3.2: Velocity triangles for a co-rotating and counter-rotating configuration: HP rotor followed by LP vane.

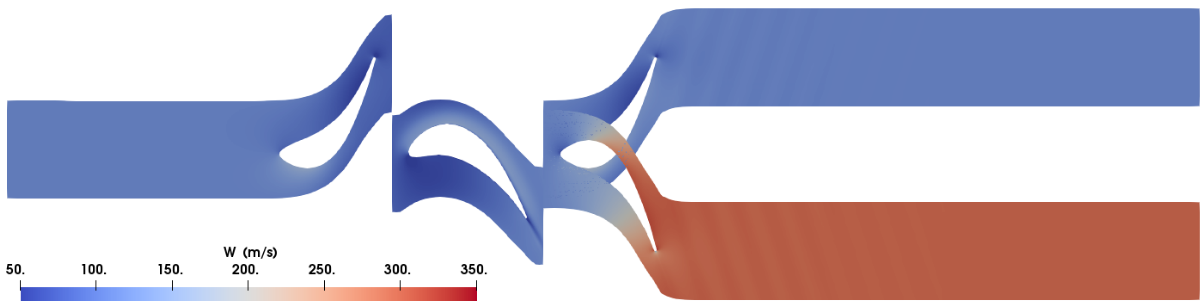

Figure 3.3: Visualization of the relative velocity field from steady simulations performed within this study. The co-rotating and counter-rotating domains are superposed.

remained unvaried. Such procedure leads to a geometry that is very similar to a linear turbine cascade, in the sense that the mean plane curvature is extremely low: however, the cascade would not have been recognized by the turbomachinery specific software employed for the simulations, as it does not have a rotating component. Instead, the present adaptation preserves the rotating nature of a standard axial turbine and is therefore accepted by the elsA software. In the following, this solution will often be referred to as "cascade", to differentiate it from the geometry with the original radius, but it should always be kept in mind that it does not coincide with a real linear cascade configuration. Table 3.2 summarizes the changes applied to the original Aachen turbine: the number of blades in each row was also modified so as to retain the initial pitch.

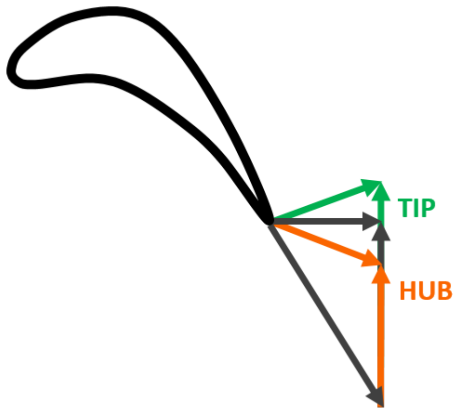

Figure 3.4: Effects of the flow incidence variation between hub and tip on the velocity triangle at the HPR exit.

	Aachen	*Cascade*
Mean radius [m]	0.2725	57.343
Rotational speed [rpm]	3500	16.63
Vane blades	36	7569
Vane blades	41	8620

Table 3.2: Geometry modifications applied to the Aachen turbine.

3.2 Numerical setup

3.2.1 Geometry and mesh

The geometry was realized with the IGG software from NUMECA. Starting from the Aachen turbine geometry, already available on NUMECA, the mean radius was extended as previously described and in one case the LP vane was mirrored with respect to the meridional plane, to create the counter-rotating configuration. Two chords were added upstream of the HP vane in order to direct the flow along an axial path. Four chords were added downstream of the LP vane so to allow the analysis of the wake decay. In order to save computational cost and time, the original 5.5 cm span was reduced[2] to 6 mm (a more detailed background on what led to this modification can be found in appendix A). Figure 3.5 shows the geometry for the co-rotating and counter-rotating case displayed on the software ParaView.

For the two configurations, two identical multi-block structured meshes were generated with AutoGrid from NUMECA: the cell distribution around the second vane is perfectly symmetrical for the two cases. The mesh covers one blade passage per row, for a total of approximately 7 million cells. A mesh convergence study was not carried out for this specific case. However, it had already been performed on a similar configuration and results were adapted to this case. The expansion ratio was always kept below 1.3, with a skewness greater than 45° on the whole domain and y^+ around 1 in the boundary layer. So as to only simulate one blade passage in the unsteady simulations (see Section 3.2.2), the blade passages were azimuthally repeated, choosing a mean value of 8095 blades for both the vanes and the rotor. In figure 3.6 a detail of the mesh including the HPV and HPR is illustrated: as the mesh is very fine, for a clearer visualization only every second point is shown.

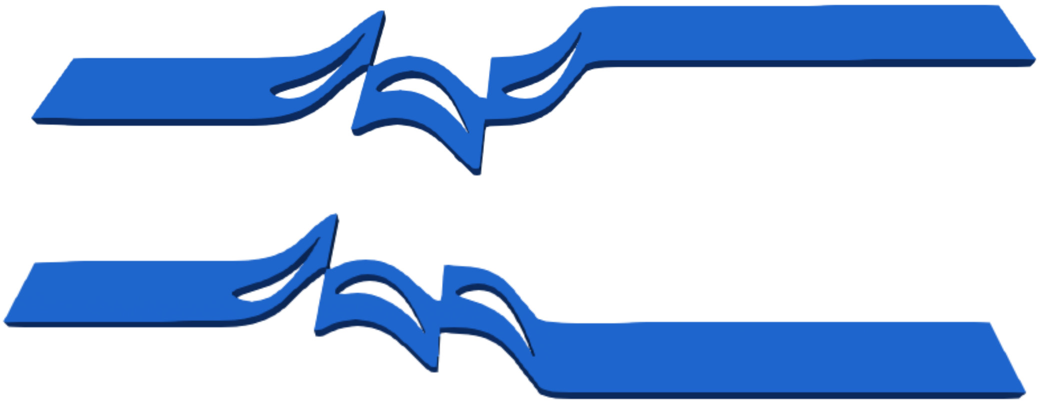

Figure 3.5: Final geometry: visualization of a single blade passage. Above, co-rotating case. Below, counter-rotating case.

[2]This significant reduction in the channel height was possible because the boundary conditions on the end-walls were always set to slip-wall, as detailed in section 3.2.3

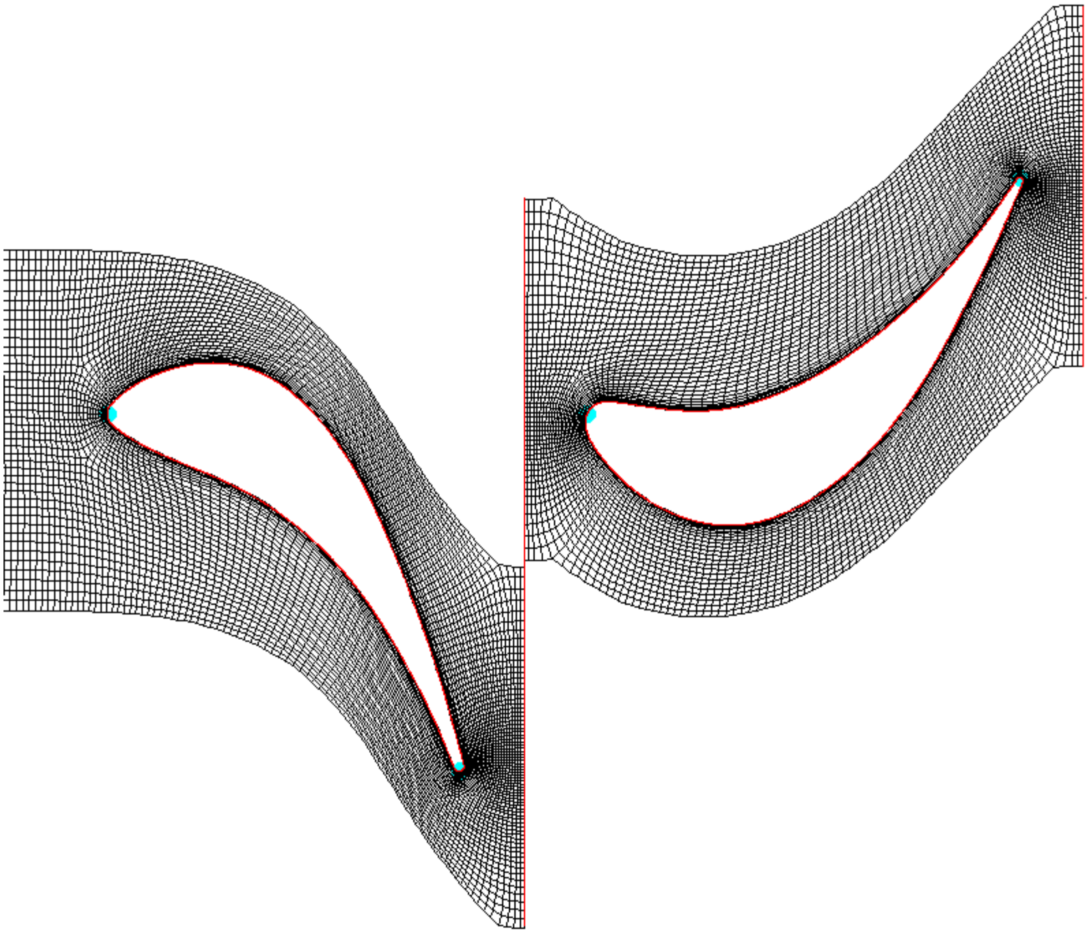

Figure 3.6: Detail of the mesh: blade-to-blade visualisation of every second grid point.

3.2.2 Numerics

As the phenomenon of the wake-mixing losses is inherently unsteady, unsteady simulations were run on the elsA software, using the PANDO supercomputer owned by ISAE-SUPAERO. The elsA software has been developed by the French research centre ONERA (*Office National d'Etudes et de Recherches Aérospatiales*) starting from 1997. It is a CFD simulation platform for multidisciplinary applications, including complex internal and external flow aerodynamics ranging from low subsonic to high supersonic regime. The elsA code relies on the solving of the compressible 3-D Navier-Stokes equations by a cell centered finite-volume method. It allows to employ the perfect gas assumption or the equilibrium real gas assumption for the fluid thermodynamic properties. [20] In this work, the ideal gas law was used, as air was set as the flowing fluid. What makes the elsA software especially suitable for turbomachinery applications is the possibility to use different formulations when simulating the flow around moving bodies: indeed, this allows the use of variables both in the absolute and in the relative reference frame. The code is based on three programming languages: C++, Fortran and Python.

To begin, steady simulations were run adopting the Mixing Plane (MP) approach[3] for the treatment of the interface between adjacent blades. The restart files from these calculations were used to initiate the unsteady simulations, which employed the RNA method[4]. In the following, the RNA method will also be referred to as Sliding Mesh (SM), which is more widely known and is based on the same principle, although the numerical implementation is slightly different. Jameson's numerical second order convective flux scheme [22] was used for spatial discretization. The Wilcox k-ω turbulence model [23] was used, as generally recommended for turbines applications, being a good compromise of accuracy and stability. However, extremely low turbulence values were set at the inlet, in order to minimize turbulent diffusion, which modifies the mixing process characteristic time scale. The inlet turbulence was defined by:

- a turbulence length scale of 0.1 mm;
- a turbulence intensity of 0.1%.

For the unsteady simulations, the implicit Gear's scheme [24] was used to guarantee second order accuracy for the approximation of the time derivative. The number of iterations per period was initially set to 80: however, mass flow convergence was compromised, so the value was doubled and finally a time step convergence was carried out between 160 and 240 iterations per blade passing period. As shown in appendix B, there was no considerable difference between the entropy fluctuations resulting from the simulations performed with these two values, and the same can be said about the static pressure fluctuations, which are not shown. Since the investigated phenomenon is relatively small and the difference in computational cost between the two values was not significant, a time discretization of 240 time-steps per blade passing period was retained.

---

[3]The Mixing Plane method consists of assuming steady flow in the appropriate frame of reference for both the vane and the rotor, and capturing the interaction between the two adjacent rows by coupling the tangential averages on both sides of the interface. It thus filters the rotor-stator interaction.

[4]The RNA method (which in French stands for *Réduction de Nombre d'Aube*, reduction in the number of blades) has been implemented by ONERA on the elsA code to perform unsteady numerical simulations for turbomachinery. It follows the principle introduced by Fourmaux [21], which allows to base the computational domain on a single blade-to-blade passage for each row, keeping the blade counts unchanged. Spatial periodicity is imposed on azimuth frontiers.

3.2.3 Initial and boundary conditions

Regarding the initial conditions, steady simulations were started from uniform flow field. Once convergence was achieved, the data were used to initiate the unsteady simulations.

To avoid the development of secondary flows, slip-wall boundary conditions were set on the end-walls. Concerning the outlet boundary conditions, for every configuration the outlet back pressure value was set so to align the flow downstream of the HPR with the axial direction. Moreover, the following inlet boundary conditions were applied to all the simulations that were carried out, as suggested by the NUMECA Tutorial for the Aachen turbine [25]:

- Inlet total temperature: 305.75 K
- Inlet total pressure: 169500 Pa
- Inlet Mach number: 0.15

Two different configurations were analysed, both for the co-rotating and counter-rotating case (figure 3.7):

1. Slip-wall boundary conditions on the surface of the vanes, adiabatic boundary conditions of adherent wall on the surface of the rotor blade. The HPV-HPR interface is treated with the Mixing Plane approach, while for the HPR-LPV interface the Sliding Mesh is employed.
   This configuration isolates the losses associated to the wake that generates from the rotor boundary layer, in order to analyse its behaviour as it passes through the downstream vane. The absence of boundary layers on the vanes allows to quantify the losses occurring as the rotor wake is segmented by the downstream vane and as it is mixed out with the rest of the fluid by viscosity. The mixing plane is used for the treatment of the first interface to reduce computational costs, as there are no unsteady phenomena propagating from the first vane.

2. Adiabatic boundary conditions of adherent wall on the surface of all the three blades. Both interfaces are treated with the Sliding Mesh approach.
   In this second configuration, the presence of the boundary layers around the two vanes allows for a more realistic study. Moreover, it permits to evaluate the significance of the wake-mixing losses in the presence of other loss sources.

In the following chapter, which shows the outcomes of the simulations, the two options just introduced will be referred to respectively as configuration 1 and configuration 2.

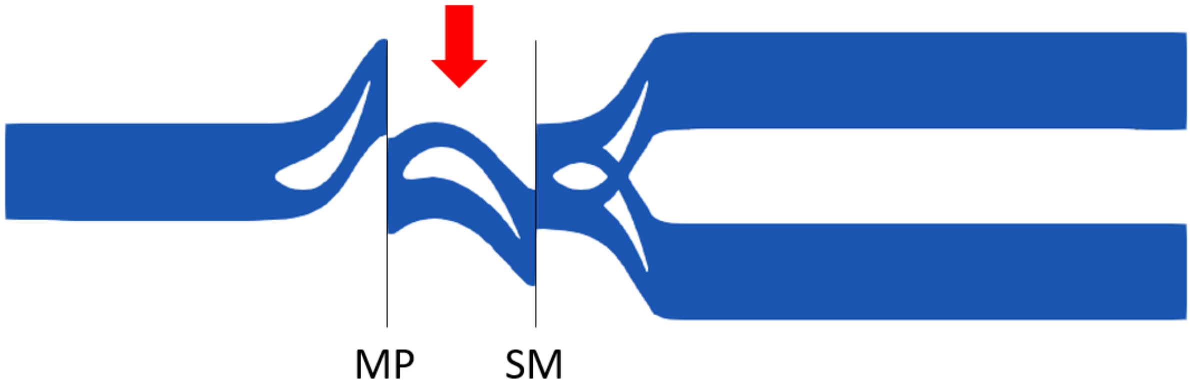

(a) Configuration 1

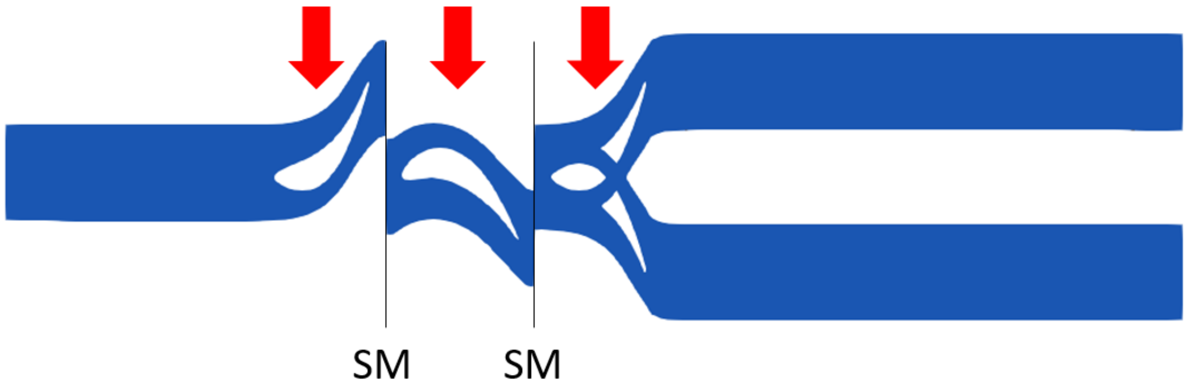

(b) Configuration 2

Figure 3.7: Blade-to-blade visualization with the co-rotating and counter-rotating domains superposed. The red arrows indicate the presence of the boundary layer on the blade's surface.

Chapter 4

Results

In the previous chapters, the subject of study has been introduced and a detailed description has been given of how the problem is addressed. Two configurations, which differ in terms of boundary conditions and interface treatment, have been presented in section 3.2.3 for the cascade geometry: in configuration 1 (figure 3.7(a)) only the rotor blades develop a boundary layer, allowing to compare the mixing-losses occurring in the co-rotating and counter-rotating case in the absence of any other source of entropy. In configuration 2 (figure 3.7(b)) both the stationary vanes and the blades are set as no-slip adiabatic walls.

In the first two sections of this chapter, the outcomes of the simulations performed on these two configurations for the co-rotating and counter-rotating case are presented. Results are expressed in terms of entropy increase, as encouraged by Denton [3] in his landmark paper on loss mechanisms in turbomachinery. The same analysis has also been carried out on the total pressure losses ξ, however results related to this variable are shown in appendix D. In the last section, a more realistic case study is briefly discussed.

Firstly, convergence was achieved for all the four unsteady simulations, meaning that the mass flow and the residuals were fluctuating periodically with a constant pattern (see appendix B). Secondly, a simulation of a single blade passage was run so to extract the values of all the useful variables. Data were extracted every two inner iterations, with a total of 120 extractions in one blade passage. All the post-processing operations were carried out using an in-house modified version of Antares, a Python Data Processing library conceived for Computational Fluid Dynamics [26]: the several "Treatments" implemented on Antares allowed to perform cuts in different directions and extract data from the obtained volumes and surfaces. The data were then either imported on ParaView, in order to display the evolution of physical quantities in space and time across the domain, or further processed on MATLAB for a more quantitative analysis.

To measure the entropy increase and the total pressure losses across the turbine rows, cuts normal to the rotation axis were made every 0.5 mm along the whole domain. On each of the obtained 2D surfaces, the mass flow averaged value of each variable at each time-step was calculated. Figure 4.1 shows the fluctuations in the flow incidence angle α at the interface between the HPR and LPV blocks over one blade passage. Clearly fluctuations are higher in configuration 2, where both the wake of the HPV and of the HPR are present, causing a more important distorsion of the flow at their passage. However, in both configurations the evolution of α is almost identical for the co-rotating and counter-rotating case, and the time-averaged value over a single blade passage is really close to zero, as specified in table 4.1. This condition was achieved by adjusting the outlet back pressure value of every simulation until the flow at the HPR exit was perfectly aligned with the axial direction. This allows to avoid any bias in the results that will be shown hereafter, which compare entropy production in the co-rotating and counter-rotating case.

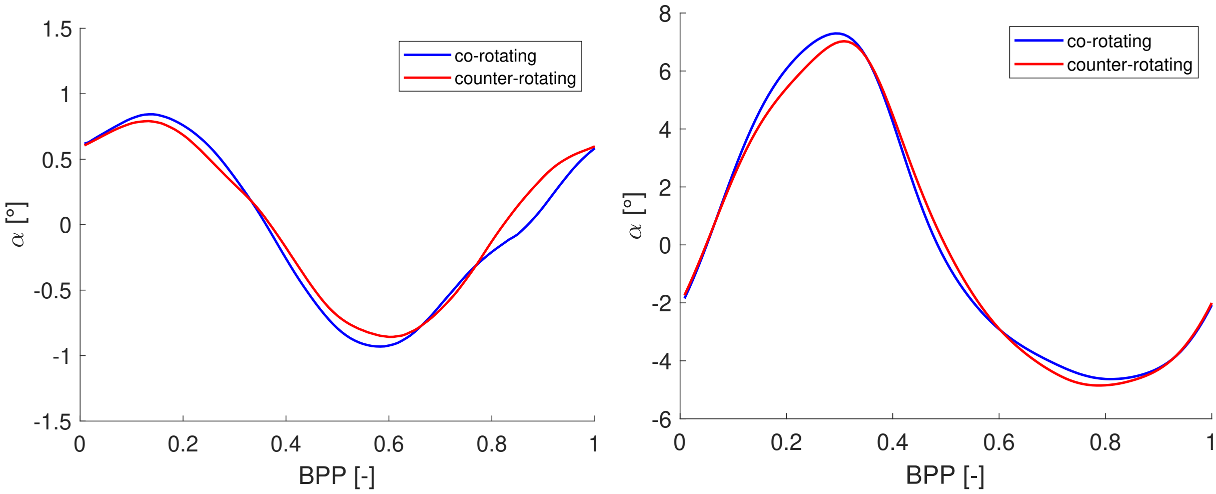

(a) Configuration 1 (b) Configuration 2

Figure 4.1: Evolution of the flow incidence angle over one blade passage at the HPR-LPV interface.

Results are shown firstly for configuration 1 and then for configuration 2. As the flow variables in the HP stage remain the same for the co-rotating and counter-rotating case, in most of the plots only the axial coordinates starting from the HPR-LPV interface are displayed in the graphs. The axial coordinates are normalised with the HPR chord and the HPR trailing edge is set as the origin of the axis.

Config.	1	2
α_{co}	-0.014°	0.158°
$\alpha_{counter}$	0.023°	0.071°

Table 4.1: Flow incidence angle at the interface between the HPR and the LPV for each configuration. Values are mass flow averaged and time-averaged over one blade passage.

4.1 Configuration 1

Figure 4.2 illustrates the instantaneous entropy distribution on a cylindrical surface at mean radius. The images clearly show the difference in wake behaviour between the co-rotating and counter-rotating case. In the former, the wakes are segmented as they pass through the LP vane, generating a certain disturbance that is amplified as the segments convect through the blades. Even at the domain outlet, four chords downstream of the LP vane, the wakes are still distinguishable from the free-stream, meaning that the disturbance is still present. Instead, in the counter-rotating case, the wakes are stretched by the downstream row, leading to a more uniform entropy distribution.
The wake behaviour in the co-rotating case is in agreement with the representation introduced by van de Wall et al. [10] for turbine flows: the length of the disturbance is reduced as it passes through the vane, while its depth is increased by a reversible flow process, as shown in the bottom part of figure 4.3(a). Concerning the counter-rotating case, a parallel can be drawn between the evolution of the wakes' shape shown in figure 4.2 and the scheme illustrated in the bottom part of figure 4.3(b), which is related to wake decay in compressors: indeed, the wake size increases in length and decreases in thickness. In their work, van de Wall et al. [10] compare the evolution of wake segments across the downstream row to the compressing or stretching of a wake in a duct of decreasing or increasing section respectively, as schematized in the top part of figures 4.3(a) and 4.3(b). These considerations follow the model introduced by Smith [16] which applies the Kelvin's theorem on a loop around the wake half width (indicated with C in figure 4.3). Under the assumption of two-dimensional, incompressible, inviscid flow, the circulation around such contour remains constant as the wake propagates: this explains why an increase in the length of the wake segment leads to a reduction of its depth - and therefore to smaller losses - and viceversa. Despite being a solely qualitative result, the entropy distributions displayed in figure 4.2 suggest that the effects of the downstream row in the counter-rotating case could be close to those of compressors, meaning that some recovery takes place as the wake segments convect through the vanes.

Figure 4.2: Configuration 1. Instantaneous entropy distribution at 50% span.

This is confirmed by the plots that follow. Figures 4.4(a) and 4.4(b) show the entropy fluctuations for the co-rotating and counter-rotating case respectively: the solid coloured line represents the mass flow averaged entropy value at a certain instant in time, while the black dashed lines indicate the envelope, meaning the maximum and minimum values reached within the entire blade passage at a certain axial coordinate. The thinner vertical lines represent the location of the LPV leading and trailing edges. What emerges is that fluctuations are more contained in the counter-rotating case: this is even more evident in figure 4.5, which compares the entropy variation within a blade passage for the two cases.

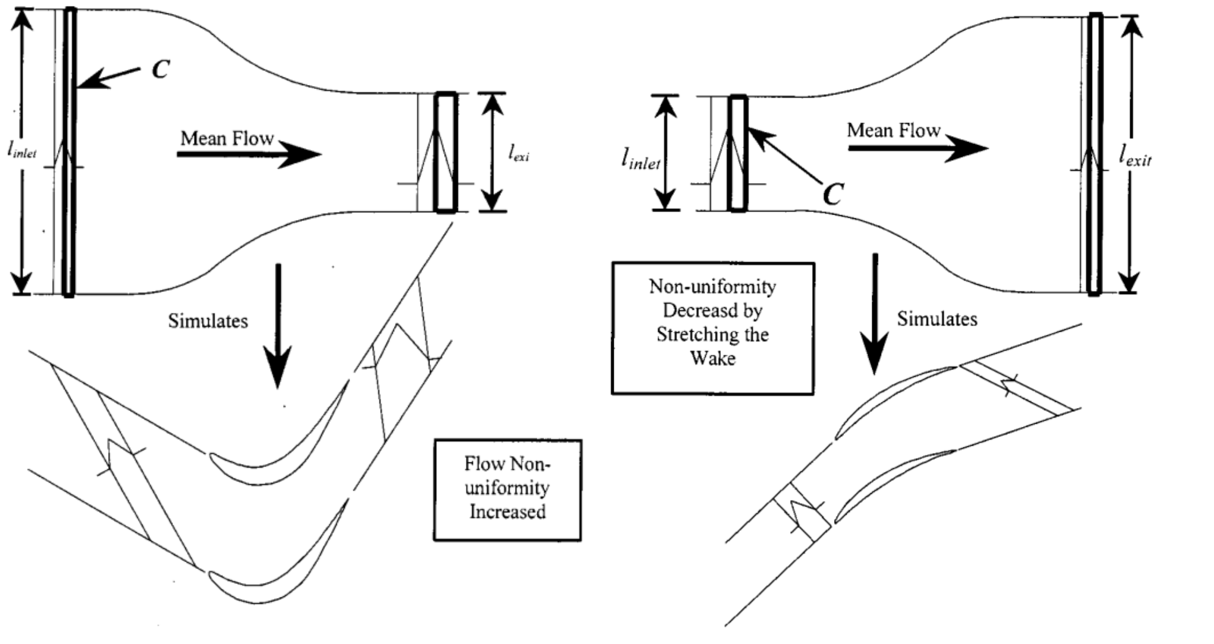

(a) (b)

Figure 4.3: (a) Turbine flow simulated by a wake compressing in an accelerating duct. (b) Compressor flow simulated by a wake stretching in a diffusing duct. [10]

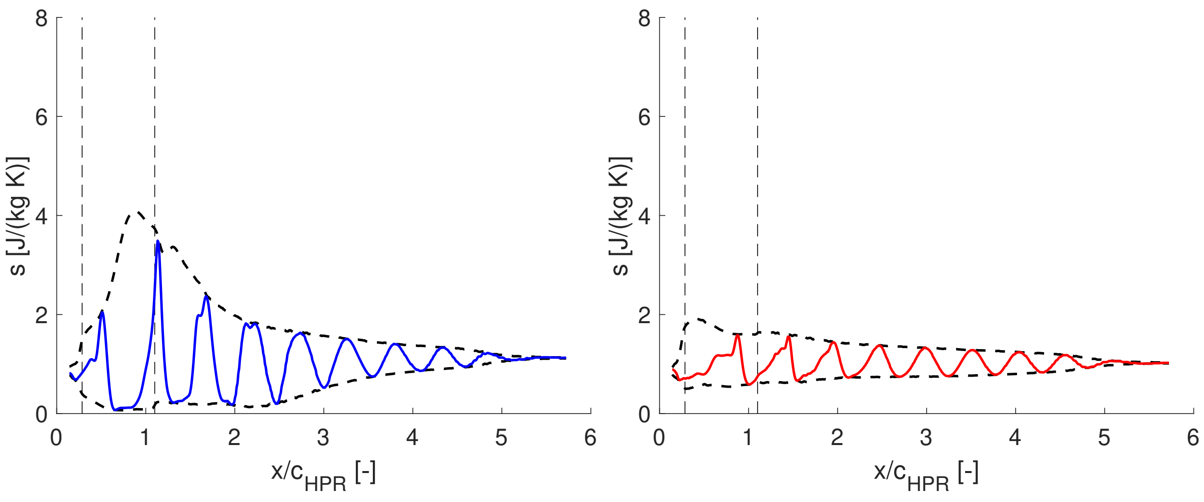

(a) Co-rotating case (b) Counter-rotating case

Figure 4.4: Configuration 1. Entropy instantaneous value and envelope in the LPV block.

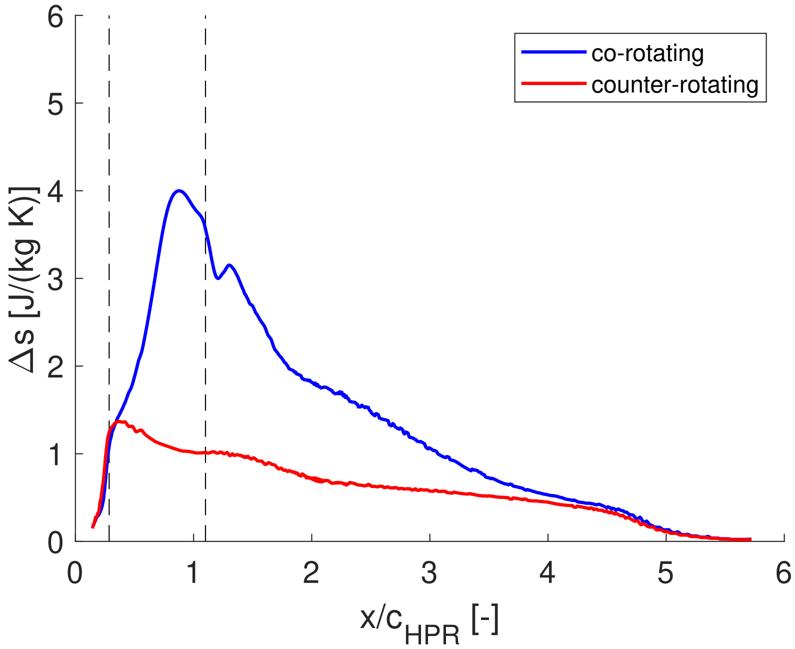

Figure 4.5: Configuration 1. Entropy variation within one blade passage in the co-rotating and counter-rotating case.

A relevant result is plotted in figure 4.6, which shows the entropy value at each axial coordinate, averaged in time over one blade passage. What appears is that entropy production is practically the same in the two cases as the flow passes across the vane, while an increasing gap generates after the vane trailing edge, as a consequence of the difference in the entropy fluctuation amplitude. The sudden entropy increase in correspondence of the trailing edge is attributable to the fact that, despite the slip-wall boundary condition on the vane surface, a small wake is still generated due to the velocity gap between the flow at the suction and pressure side. Looking at the entropy trend downstream of the vane, it is apparent that the passing of the wake through the vane of the co-rotating turbine results in greater losses: this means that the wake-mixing losses are amplified by this geometry. Contrarily, in the counter-rotating configuration entropy stays approximately constant downstream of the LP vane, meaning that, thanks to its interaction with the downstream row, the disturbance is almost completely attenuated.

The gap in entropy variation across the LP vane between the co-rotating and counter-rotating case can be evaluated by comparing the following normalized parameter:

$$\Delta \hat{s} \ [\%] = \frac{\Delta s_i}{\Delta s_{HPR}} \cdot 100. \tag{4.1}$$

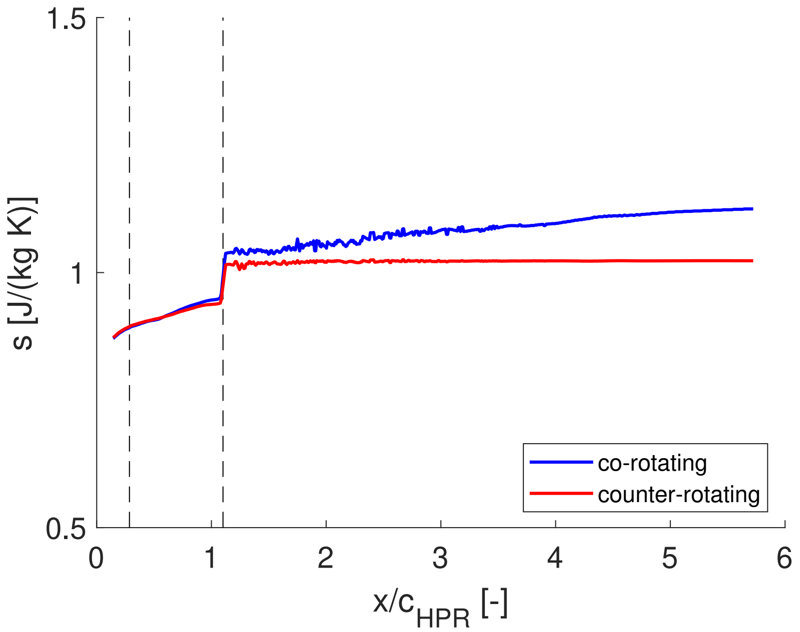

Figure 4.6: Configuration 1. Entropy production trend in the co-rotating and counter-rotating case.

Δs_i indicates the entropy production occurred between the rotor trailing edge and a certain station located i chords downstream of the LPV trailing edge, while Δs_{HPR} is the entropy increase that takes place as the flow passes across the HP rotor. Table 4.2 indicates the values of such parameter at different coordinates for the co-rotating and counter-rotating case. It can be concluded that the losses caused by the mixing of the HP rotor wakes are smaller if the downstream row belongs to a counter-rotating turbine stage: the difference in entropy generation between the two cases amounts to 12% of Δs_{HPR} at the outlet.

i	1	2	3	4
$\Delta\hat{s}_{co}$ [%]	27	30	32	35
$\Delta\hat{s}_{counter}$[%]	23	23	23	23

Table 4.2: Difference in entropy variation between the co-rotating and counter-rotating case. i indicates the number of chords downstream of the LPV trailing edge.

To better observe the impact of the wake-mixing losses, it can be useful to compare the entropy generated in the steady and unsteady simulations for configuration 1. Figure 4.7 shows the entropy variation across the whole domain for steady and time-accurate simulations both for the co-rotating and counter-rotating case. As expected, the losses

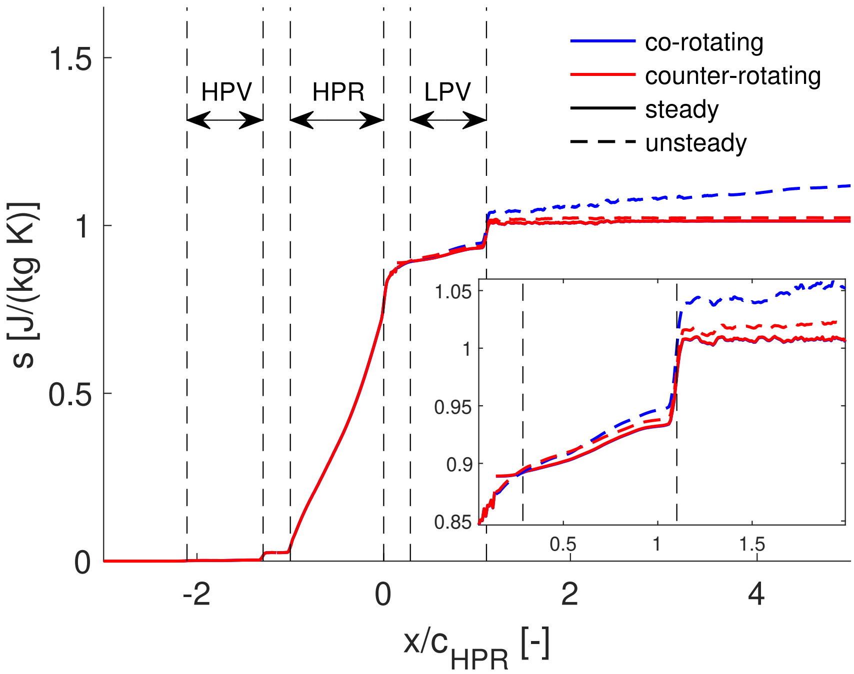

Figure 4.7: Configuration 1. Entropy production obtained in steady and unsteady simulations for the co-rotating and counter-rotating case. For unsteady simulations, only values of the LPV block are plotted.

recorded in the steady simulations are exactly the same for the two cases: indeed, the variables at the row interfaces are tangentially averaged, so there are no wakes propagating in the LP vane. The use of the mixing plane also explicates the small entropy jump at the HPR-LPV interface observed for the steady case, which is a consequence of the averaging operation. The difference between the solid lines and the dashed lines in the graph, indicating respectively the entropy produced in the steady and unsteady case, is representative of the entropy exclusively associated to the mixing-losses. Both in the co-rotating and in the counter-rotating case, the introduction of this unsteady phenomenon brings about a certain amount of loss: however, in the counter-rotating case the additional losses do not increase as much as in the co-rotating case as the wakes pass across the LP vane. Furthermore, losses remain constant downstream of the LP vane in the former case, while in the latter they keep increasing almost linearly until the domain outlet. This is highlighted in the plot of figure 4.8, which represents the entropy production gap between steady and unsteady simulations.

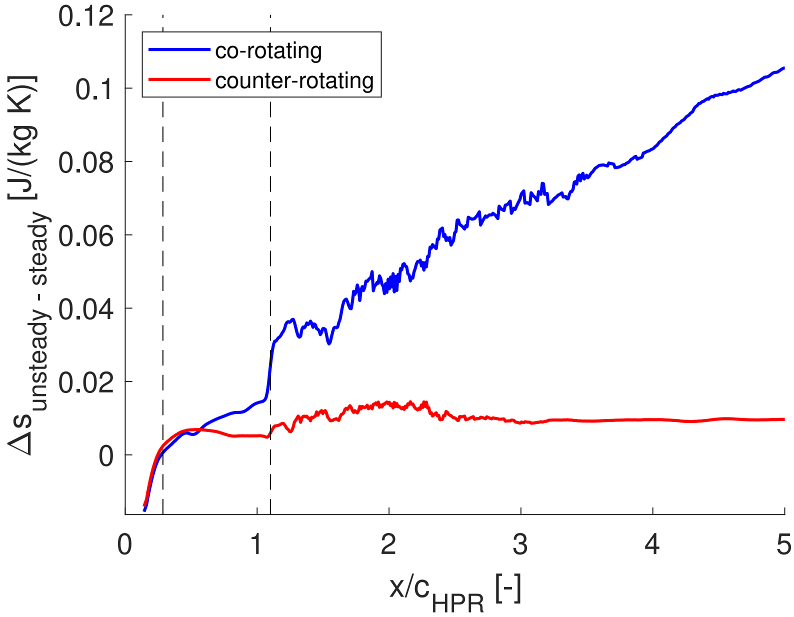

Figure 4.8: Configuration 1. Difference in entropy production between steady and unsteady simulations for the co-rotating and counter-rotating case.

4.2 Configuration 2

Figure 4.9 shows the instantaneous entropy distribution at mean radius for configuration 2. In this case, all the rows have no-slip adiabatic boundary conditions on the blade surfaces, so the decay of the rotor wakes is also influenced by their interaction with the wakes that generate from the HP vane and with the LP vane boundary layers. It can be seen that the wakes generating from the vanes are thicker and lead to higher losses than the rotor wake: this is due to the fact that the vane trailing edge is more than 1.5 times thicker than the rotor trailing edge[5]. Just like in configuration 1, the wakes in the counter-rotating case disappear more rapidly, while in the co-rotating one the interaction between the rotor wake segments and the LPV wakes originates some areas of higher entropy.

The entropy fluctuation trend seen in the two cases for configuration 1 is replicated in configuration 2 (figure 4.10): overall, both the co-rotating and counter-rotating case present greater losses than the respective cases of the previous configuration, due to the presence of the vane boundary layers. However, the difference in oscillation amplitude

[5]The fact that rotor blades have a thinner trailing edge is a common feature in turbines: since rotors are subject to elevated rotational speeds and high loads, they undergo higher precision manufacturing processes than the stationary vanes.

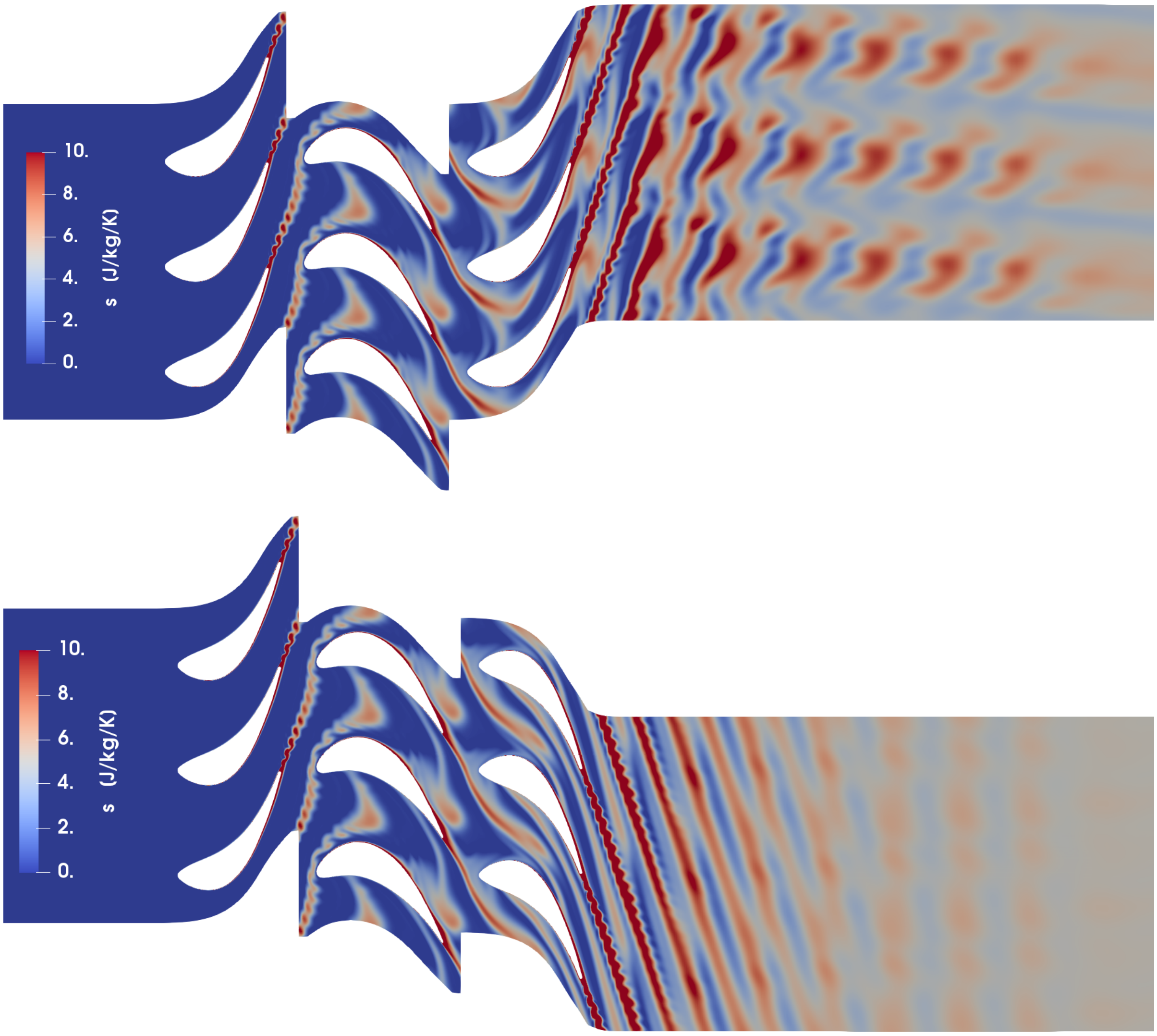

Figure 4.9: Configuration 2. Instantaneous entropy distribution at 50% span.

between figure 4.10(a) and 4.10(b) is still visible, meaning that the phenomenon is not completely hidden by the additional losses which characterize this configuration. This is confirmed by the time-mean entropy values plotted in figure 4.12. Furthermore, figure 4.13 proves that the absolute advantage brought by the counter-rotating case in terms of wake-mixing losses is still there in the presence of a boundary layer on the vanes. In this plot, the time-mean entropy of the counter-rotating case has been subtracted from the one of the co-rotating case, both for configuration 1 and 2. In this way, the losses related to wake-mixing are isolated and compared. What emerges is that the absolute advantage of the counter-rotating turbine in terms of entropy generation is even slightly higher for configuration 2: indeed, at the domain outlet the difference in entropy production between the two cases is of about 17% of Δs_{HPR}, compared to 12% of configuration 1.

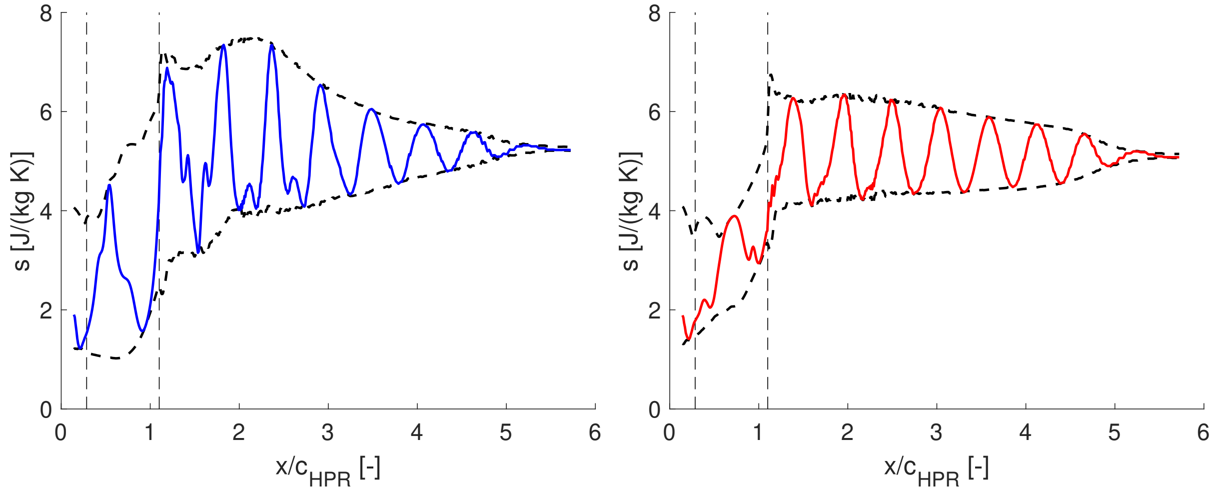

(a) Co-rotating case (b) Counter-rotating case

Figure 4.10: Configuration 2. Entropy instantaneous value and envelope in the LPV block.

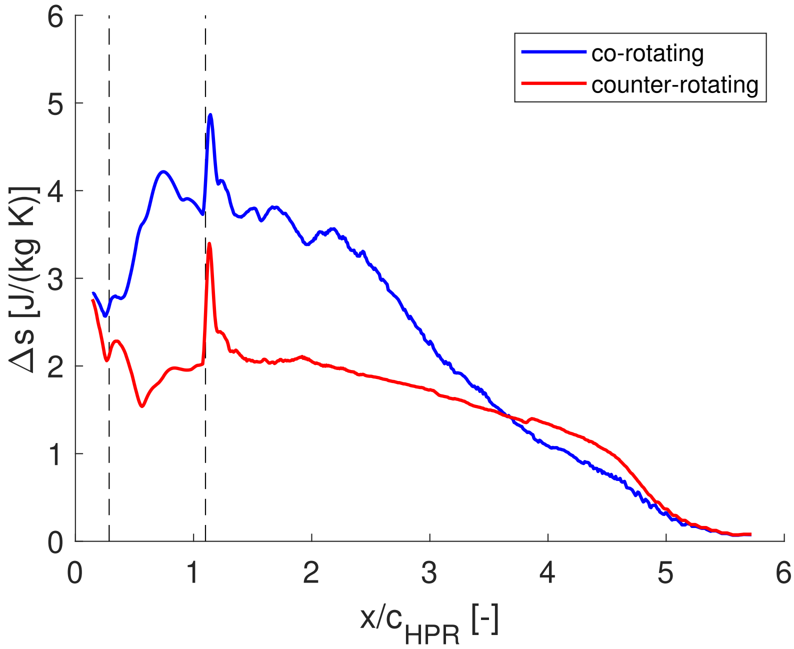

Figure 4.11: Configuration 2. Entropy variation within one blade passage in the co-rotating and counter-rotating case.

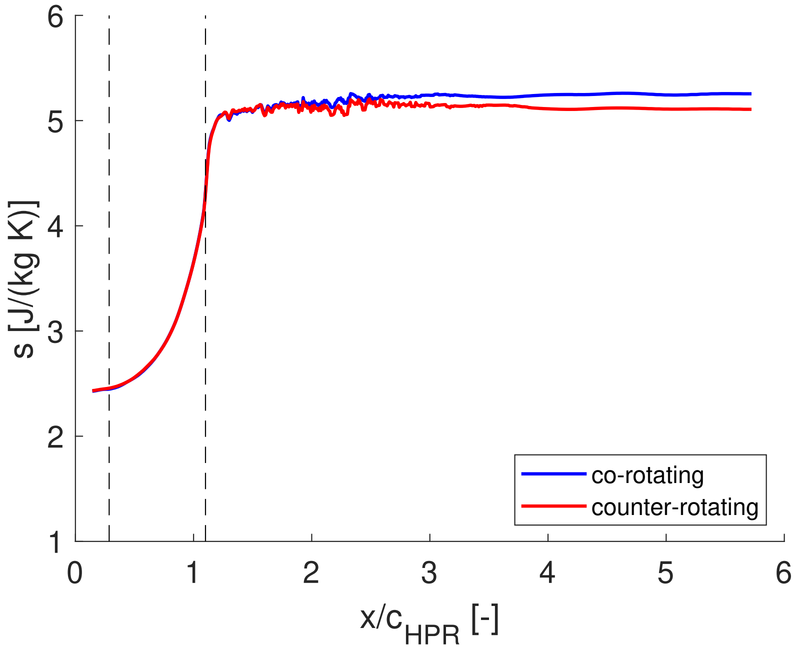

Figure 4.12: Configuration 2. Entropy production trend in the co-rotating and counter-rotating case.

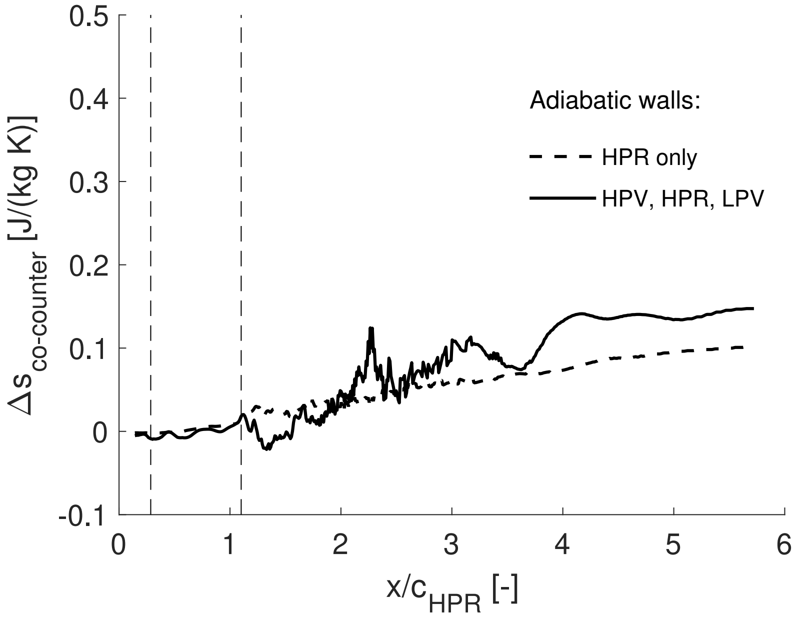

Figure 4.13: Difference in time-averaged entropy between the co-rotating and the counter-rotating case, for configurations 1 (HPR only adiabatic walls) and 2.

Finally, figures 4.14 and 4.15 show the difference in generated entropy between steady and unsteady calculations, as previously done for configuration 1. As seen in the first figure, a different increase in entropy occurs in steady and unsteady calculations starting from the HPV: this is due to the fact that a different outlet pressure value was set in order to have zero incidence at the exit of the HP rotor (respectively 109500 Pa and 106100 Pa for steady and unsteady simulations). What is especially relevant, however, is the gap that generates after the LP vane between the co-rotating and counter-rotating case: the entropy difference between steady and unsteady computations tends to decrease in the counter-rotating turbine, while it keeps growing downstream of the LPV in the co-rotating one.

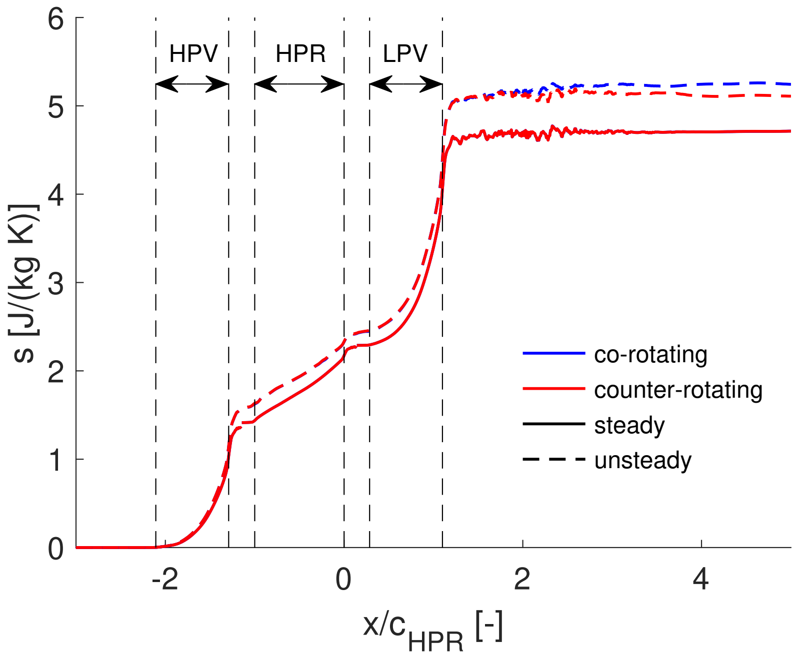

Figure 4.14: Configuration 2. Entropy production obtained in steady and unsteady simulations for the co-rotating and counter-rotating case.

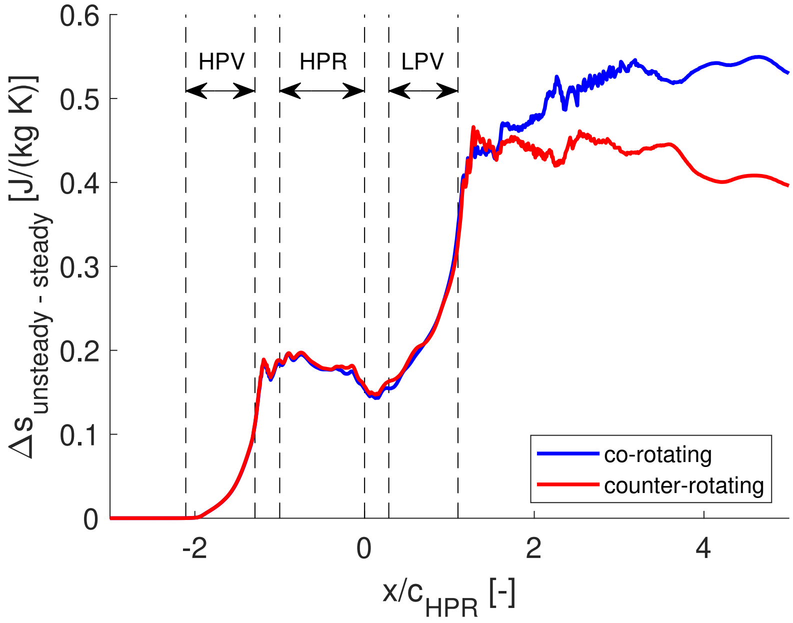

Figure 4.15: Configuration 2. Difference in entropy production between steady and unsteady simulations for the co-rotating and counter-rotating case.

4.3 Double-stage configuration

In the previous sections, the effects of the downstream vane row on wake decay have been analysed using a simplified geometry. The employed boundary conditions, along with the absence of tip-gap and the extended mean radius, have allowed to isolate the losses associated to this phenomenon in order to observe it in more detail. The subsequent step consists therefore of extending the analysis to a more realistic case study. For this purpose, further time-accurate simulations were run on a double-stage turbine obtained by adding an identical rotor downstream of the original Aachen turbine. To create the counter-rotating geometry, both the LP vane and the LP rotor were mirrored with respect to the meridional plane. The rotational speed imposed to the LPR is identical in value and opposite in direction to the one of the HP rotor. A tip-gap was added on the HPR blade and boundary conditions were set to adiabatic-wall not only on the vanes and blades but also on the hub and shroud walls. The periodicity was set to 38 for every row, as a compromise between the 36 vanes and the 41 rotor blades of the original configuration. A new mesh with 22.8 million cells was created and the numerical setup of the previous simulations (described in section 3.2.2) was retained. Figure 4.16 shows the flow incidence across the LP stage (with an inverted sign for the co-rotating case), proving that the comparison between the co-rotating and counter-rotating stage is not biased by possible differences in the flow angle.

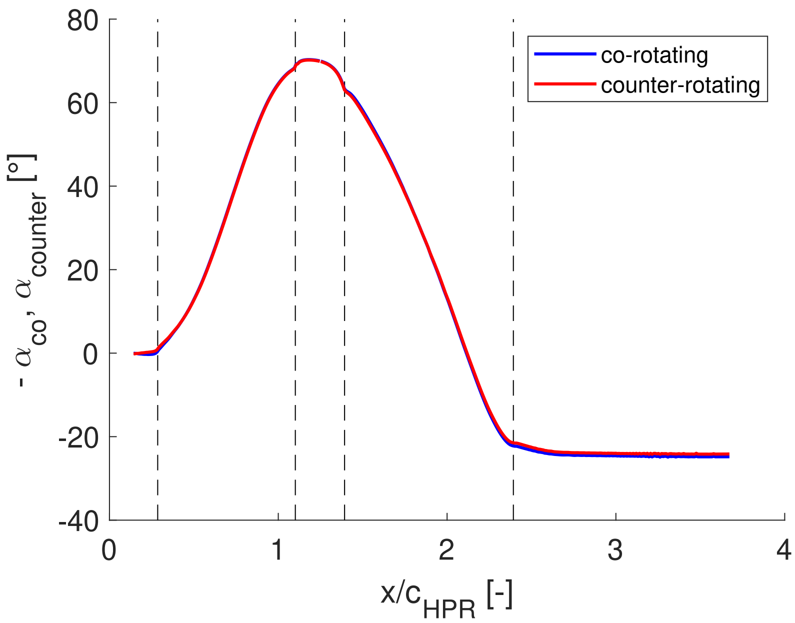

Figure 4.16: Double-stage configuration. Flow incidence angle across the LPV and LPR.

The results of this last study are summarized in figures 4.17 and 4.18. The difference in entropy fluctuations across the LP vane follows the same pattern as in the cascade case, with lower amplitudes in the counter-rotating case. This leads to higher stability in the flow entering the LP rotor. However, oscillations seem to be amplified as the flow passes through the blades of the counter-rotating LP rotor, while the opposite is seen in the co-rotating case.

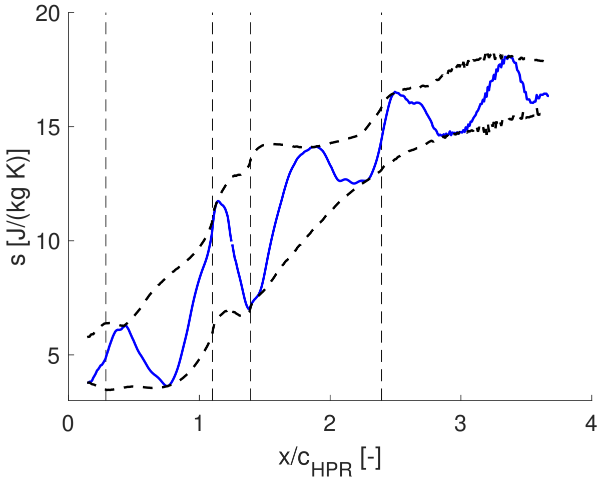

(a) Co-rotating case

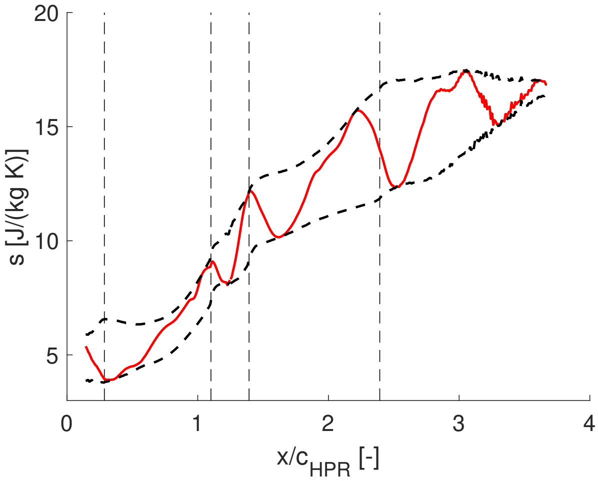

(b) Counter-rotating case

Figure 4.17: Double-stage configuration. Entropy instantaneous value and envelope for the LPV and LPR blocks.

When calculating the time-mean entropy distribution in the LP turbine domain, there is no appreciable difference between the two cases: the advantage found in the previous configurations for the counter-rotating case is not visible on this double-stage turbine. The second stage isentropic efficiency, calculated with equation 4.2, has a value of 87.234% and 87.247% respectively for the co-rotating and counter-rotating LP turbine, indicating that the difference is negligible.

$$\eta_{is} = \frac{T_{t_{in}} - T_{t_{out}}}{T_{t_{in}} - T_{t_{out}}\ \exp\left(-\frac{S_{out}-S_{in}}{Cp}\right)} \tag{4.2}$$

This can be due to the several limits of the employed geometry. First of all, the original Aachen turbine consists of a 1.5 stage design: in this final part of the study, a low-pressure rotor has been added downstream of it to study whether lower fluctuations in the LP vane could lead to an improvement in the performance of the downstream rotor. However, this results in a geometry that is not optimized. Moreover, as the channel height is limited, secondary flows interfere with a significant part of the passage section. Finally, as mentioned in section 3.1, the Aachen turbine is characterized by untwisted vanes and blades, which cause the flow incidence to vary considerably between the end-walls. All these sources of loss and asymmetry tend to hide the effects that have been appreciated in the simpler configurations.

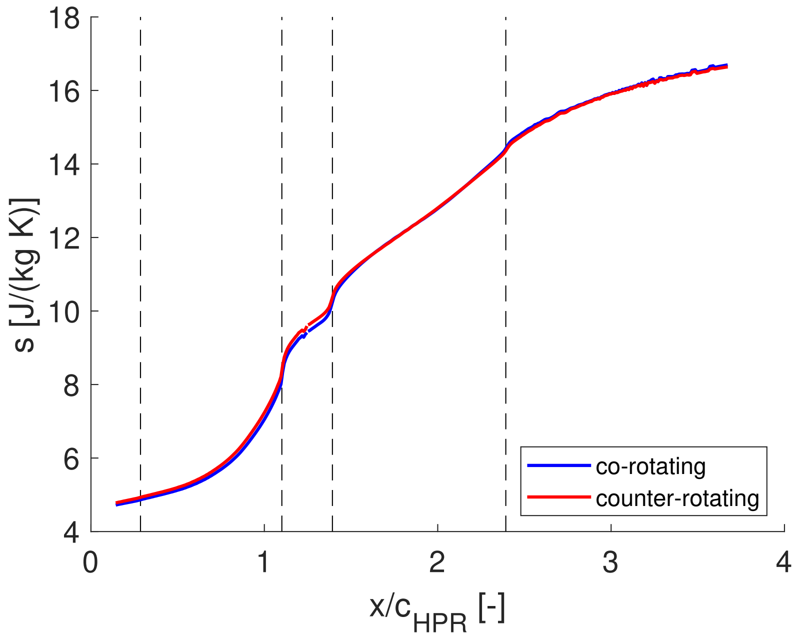

Figure 4.18: Double-stage configuration. Entropy instantaneous value and envelope for the LPV and LPR blocks.

Chapter 5

Conclusions and future perspectives

The aim of the present work has been to provide a broader understanding of the phenomenon of the mixing-losses in turbines, in order to ameliorate the design of the TVF. As contradictory information on the subject is still present in the literature, this study has been carried out in an attempt to answer the question of whether losses are amplified or attenuated as turbine wakes pass through the adjacent downstream row. To do this, numerical simulations have been performed on a co-rotating and on a counter-rotating 1.5 stage turbine: in the former case, the flow entering the LP vane is slowed down in the rotating reference frame, while in the latter case it is accelerated.

Two configurations characterized by different boundary conditions have been studied. The set up of configuration 1 has allowed to isolate the losses associated to the decay of rotor wakes from other unsteady effects and to evaluate the differences in entropy production between the co-rotating and counter-rotating geometry. A comparison has also been made between the entropy levels obtained in the steady and time-accurate simulations, to assess the entropy contribution brought by the mixing of wakes in the downstream row. In accordance with Praisner et al. [11] and van de Wall et al. [10], a reduction in the wake-mixing losses has been observed in the counter-rotating case with respect to the standard one. As the only difference between the co-rotating and the counter-rotating case is the way in which wake segments convect through the LP vane, it can be confirmed that wake stretching leads to decreased losses with respect to wake dilation. Indeed, viscosity acts to reduce the magnitude of the disturbance in the exact same way for the two cases:

what changes is the contribution brought by the inviscid mechanism set off by the presence of the downstream row.

The reduction in entropy production for the counter-rotating case, that is apparent when neglecting all other types of losses (as in configuration 1), is still evident even in the presence of an interaction between the rotor wakes and the vanes boundary layers and wakes (as in configuration 2). Configuration 2 has also led to assert that such benefit retains its absolute magnitude even in the presence of other losses.

A more realistic double-stage turbine configuration has finally been employed: however, no significant advantage has been measured for the counter-rotating case. Indeed, the entropy production in the LP stage has been found to be practically the same for the two cases and the difference in isentropic efficiency is negligible. Nevertheless, this can be due to several factors that cause the employed two-stage configuration to be unsuitable for this kind of analysis. This also legitimizes the efforts previously made in order to set up a cascade configuration, as well as the choice of boundary conditions, as it shows that otherwise it would not have been possible to discern and analyse the phenomenon.

To conclude, it can be stated that the stretching of wakes in the downstream row can lead to a reduction in entropy production: this can be explained in terms of "*relative magnitudes of the inviscid and viscous mechanisms involved*" [10] in the decay process. Indeed, entropy generation occurs as viscosity acts to mix out the non-uniformity of the flow. If a reversible recovery process takes place at the same time, it decreases the wakes depth without incurring any loss: in this case the overall losses will be smaller than if viscosity was acting alone to mix out the wakes. The opposite can be said in the case of a negative recovery, namely when the wake size is increased by an inviscid mechanism: in such circumstances, stronger viscous effects must come into play in order to even out the disturbance.

As the next step, simulations should be performed on an optimized double-stage turbine geometry, in order to evaluate the magnitude of this phenomenon on a real aircraft engine. Indeed, it has to be reminded that the final purpose of the present work is to suggest possible improvements for the design of the TVF. While the Aachen turbine is characterized by a constant passage area, the inter-turbine duct is subject to a significant section increase, thus being extremely diffusive. In a standard dual-spool turbine, two factors would therefore contribute to dilate the wakes generated by the last HP rotor as they propagate through the duct: the presence of the cambered fairings and the area increase (as already studied in a previous work). Instead, in a counter-rotating configuration the former factor would compete against the latter, partially reducing the losses. It would be interesting, in the future, to evaluate the relative importance of the two effects, so as to understand to what extent wake-mixing losses are increased in a co-rotating TVF configuration with respect to the counter-rotating one.

Appendix A

Geometry modification

Originally, the intention was to extend the mean radius of the Aachen turbine (by applying all the modifications described in table 3.2 of section 3.1) while retaining the initial span height of 5.5 cm.

A mesh was created having 23 million cells, both for the co-rotating and for the counter-rotating geometry. The span-wise cell distribution was set so to obtain $y^+ \simeq 1$ not only on the blades surface but also on the end-walls. Although the primary interest was to consider a configuration with slip boundary conditions on the end-walls so as to avoid any additional disturbance, this choice was made in order to potentially carry out simulations activating all the boundary layers, at a second stage.

However, the thickness of the first cell height at hub and tip had to be of the order of 10^{-6} in order to keep y^+ around unity. This meant having a considerable difference in order of magnitude between the tip and hub radius and the first cell height, which caused some problems in the simulations. Figure A.1 shows the results of a simulation in which the end-walls and the vane blades were set to slip walls: while the entropy distribution should have been uniform at the hub and tip of the HP vane, regions of negative entropy appeared in those areas. For this reason, the idea of activating the end-wall boundary layers on the cascade geometry was abandoned and it was decided to use a constant span-wise cell distribution. At this stage, to save computational cost and time, the domain height was reduced to 6 mm, retaining the same extended mean radius: this allowed to only employ 48 cell layers and set the cell height to $1.25 \cdot 10^{-4}$.

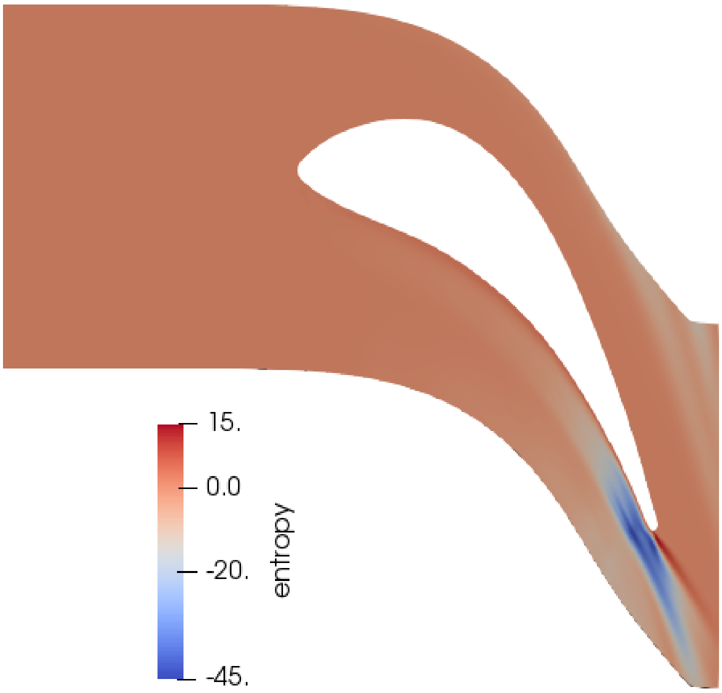

Figure A.1: Full span cascade geometry: unphysical entropy distribution at HPV hub.

Appendix B

Convergence of numerical simulations

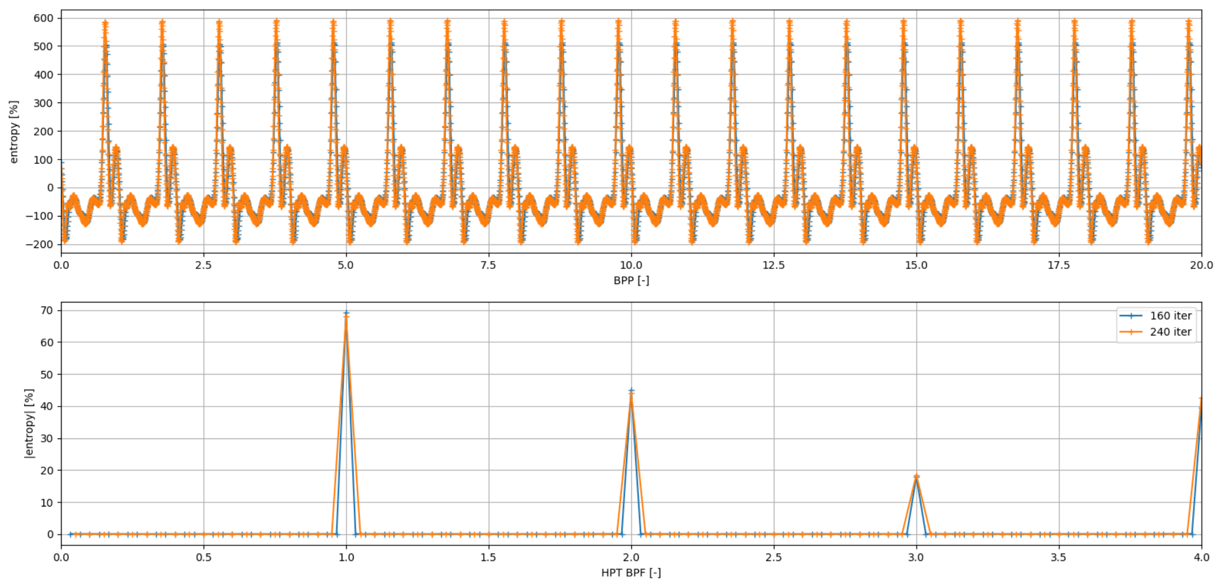

Figure B.1: Time-step convergence between 160 and 240 iterations per period. Above, entropy fluctuations one chord downstream of the LPV. Below, FFT spectrum.

In order to measure entropy and static pressure fluctuations in time, several probes were placed at different locations in the domain. Figure B.1 is referred to the co-rotating case of configuration 1 and it illustrates the entropy fluctuations measured by one of these probes for simulations with 160 and 240 iterations per period. It shows that time-step convergence is achieved, as there is no appreciable difference between the fluctuations registered in the two cases.

Figure B.2 displays the residuals of the following quantities:

- *ro* = density;
- *rou, rov, row* = x, y, and z components of momentum;
- *roE* = total energy per unit of volume;
- *roK, roEps* = first and second turbulent conservative variables.

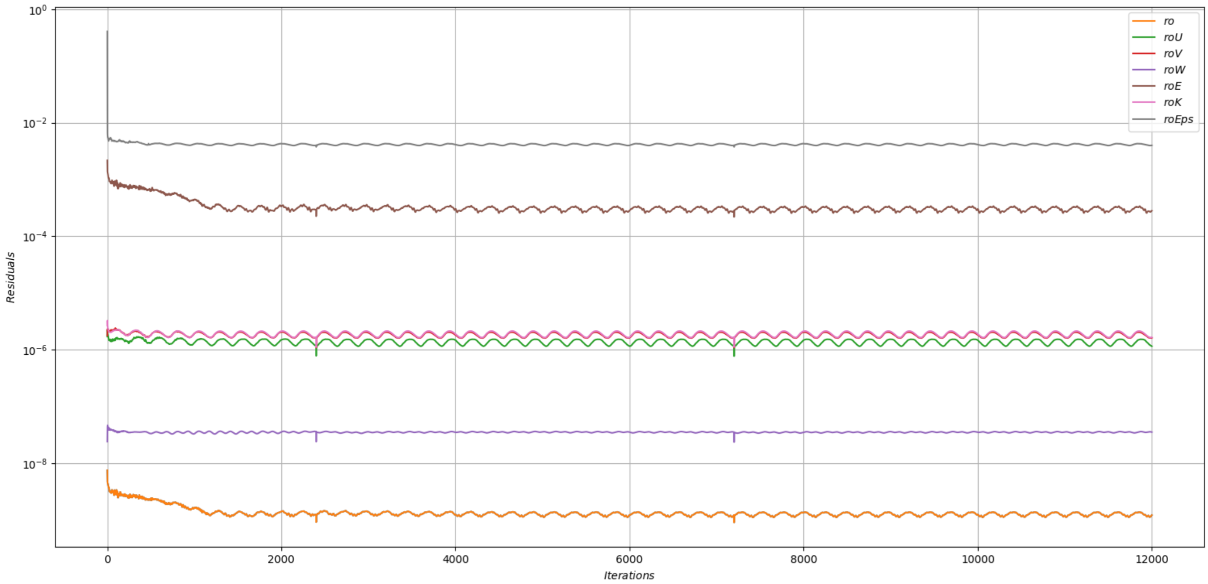

Figure B.2: Example of residuals for an unsteady simulation.

Figure B.3 shows an example of mass flow convergence for an unsteady calculation. Every mass flow fluctuation corresponds to one wake passage. As fluctuations become periodic and their amplitude is stabilized, convergence is considered to be achieved.

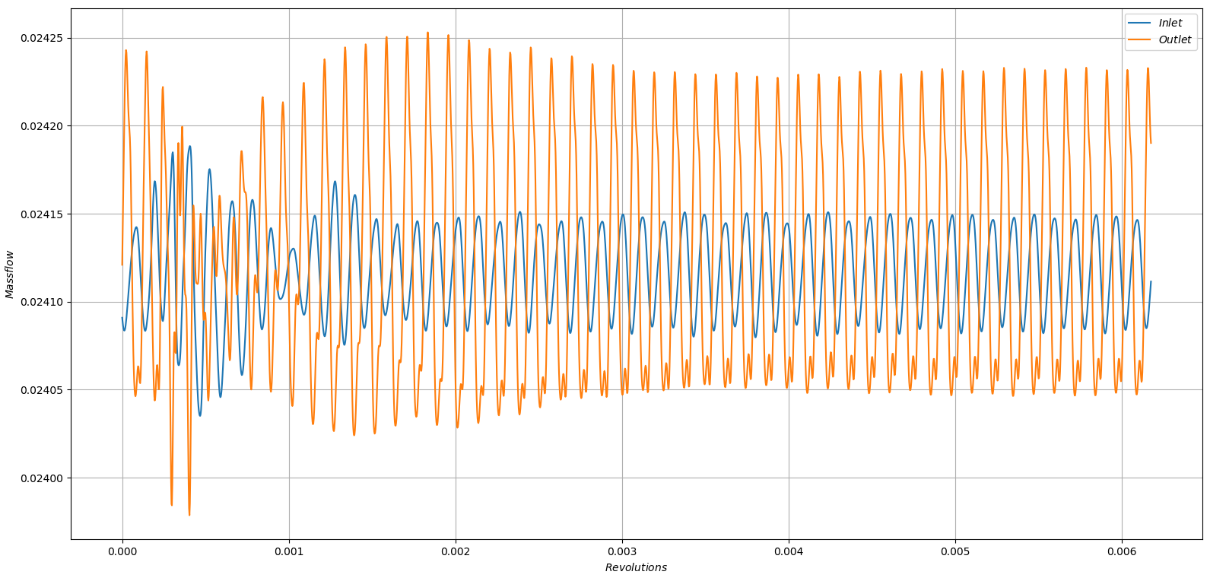

Figure B.3: Example of mass flow convergence for an unsteady simulation. Mass flow is expressed in kg/s and it is referred to a single blade-to-blade passage.

Appendix C

Code validation against esperimental data

The elsA flow solver has been used for several years by the ONERA research center, as well as by the aerospace companies Safran and Airbus, to run RANS simulations for turbomachinery applications. For this reason, there is no need for further validation of the code.

However, there is no record of employing such code on the Aachen turbine geometry: a steady simulation was therefore run using the original geometry, with the purpose of comparing experimental and numerical data. The only available experimental data are those shown by Aubé and Hirsch [19]: the authors performed calculations on the Aachen turbine at different operating points and validated their results through experimental measurements. Their comparison was carried out on the span-wise variation of the absolute flow angle at different stations along the domain and the results were overall satisfactory. When comparing this variable, it can be stated that the outcomes of the steady simulation carried out within the present study are in line with those obtained by Aubé and Hirsch both numerically and experimentally. As shown in figure C.1, in the two plots the flow incidence varies in the same manner along the radial direction. The difference in the values of α is due to a difference in mass flow.

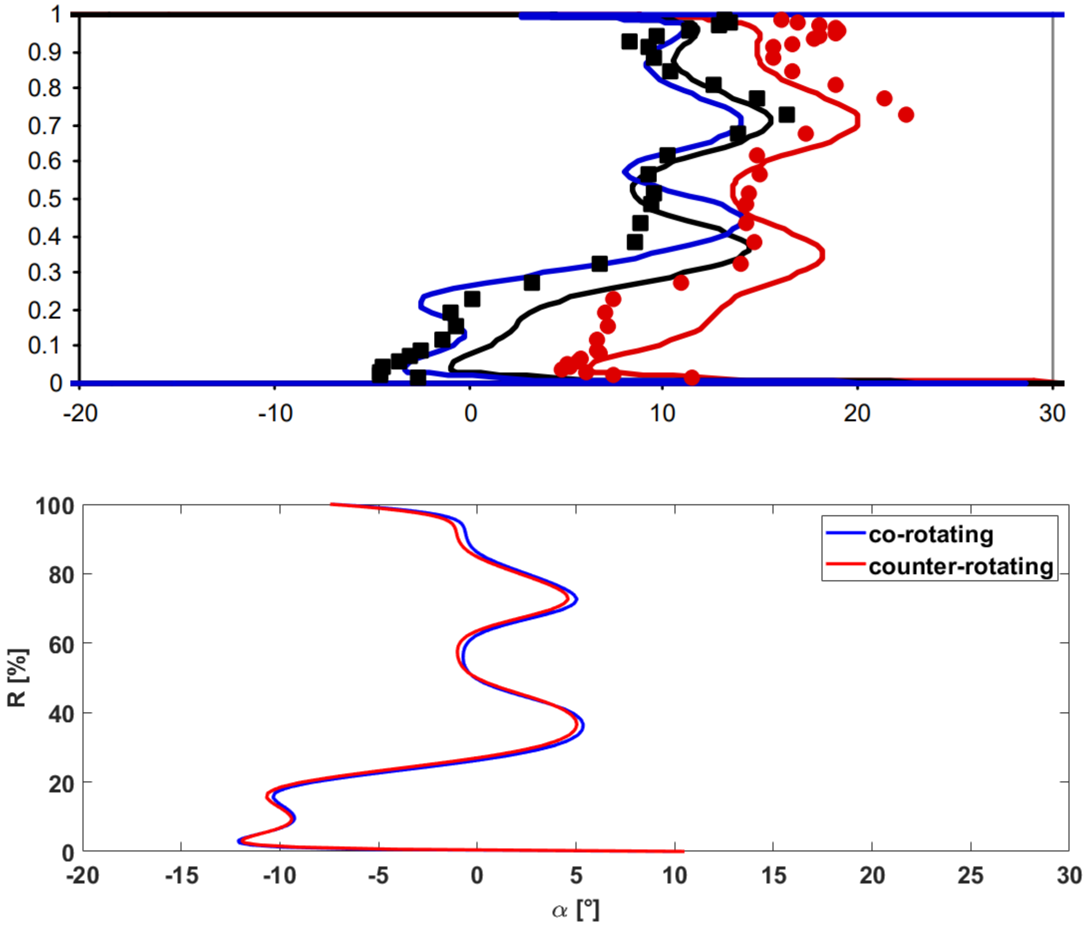

Figure C.1: Pitch-averaged absolute flow angle span-wise variation downstream of the rotor. Above, experimental and computational results from [19] for different mass flow values. Below, computational results from the present study.

Appendix D

Results in terms of total pressure losses

In chapter 4, results have been shown with regard to entropy production, comparing the entropy increase taking place in the co-rotating and counter-rotating case. In this section, results are proposed in terms of total pressure losses, following the definition of Praisner et al. [11] (section 2.2). Figure D.1 shows a reduction in total pressure fluctuations for the counter-rotating case with respect to the co-rotating one, similarly to what has been observed regarding entropy fluctuations. The same consideration applies to configuration 2, as plotted in figures D.5. A comparison between the total pressure fluctuations in the co-rotating and counter-rotating turbine can also be made in terms of Root Mean Square values: plots D.4 and D.8 compare the maximum and mean RMS fluctuations, normalized with the mean total pressure value, for configurations 1 and 2 respectively, denoting more stability in the pressure field of the counter-rotating stage.

Moreover, it can be seen in figure D.3 that the total pressure jump across the LP vane and downstream of it is higher in the co-rotating case. However, this difference becomes negligible in configuration 2 (figure D.7), where the total pressure jump is much higher due to the presence of the LPV boundary layer.

Finally, regarding the double-stage configuration (figure D.9), pressure oscillations across the LPV are more contained in counter-rotating case: however, they are amplified as the flow passes in the LPR, while the opposite seems to happen in the co-rotating case. The fluctuation peaks towards the domain outlet are comparable for the two cases.

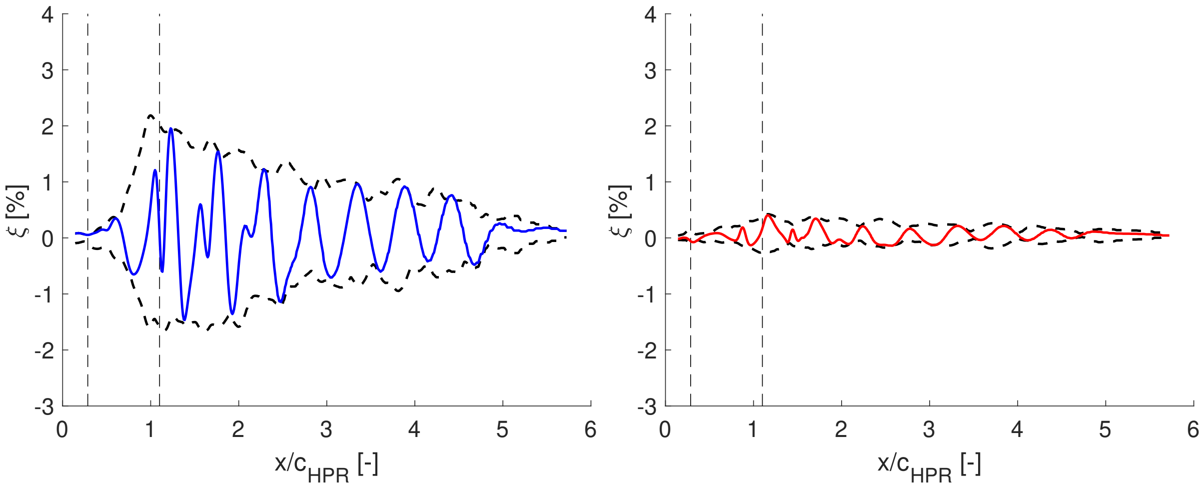

(a) Co-rotating case

(b) Counter-rotating case

Figure D.1: Configuration 1. Instantaneous value and envelope of the total pressure losses in the LPV block.

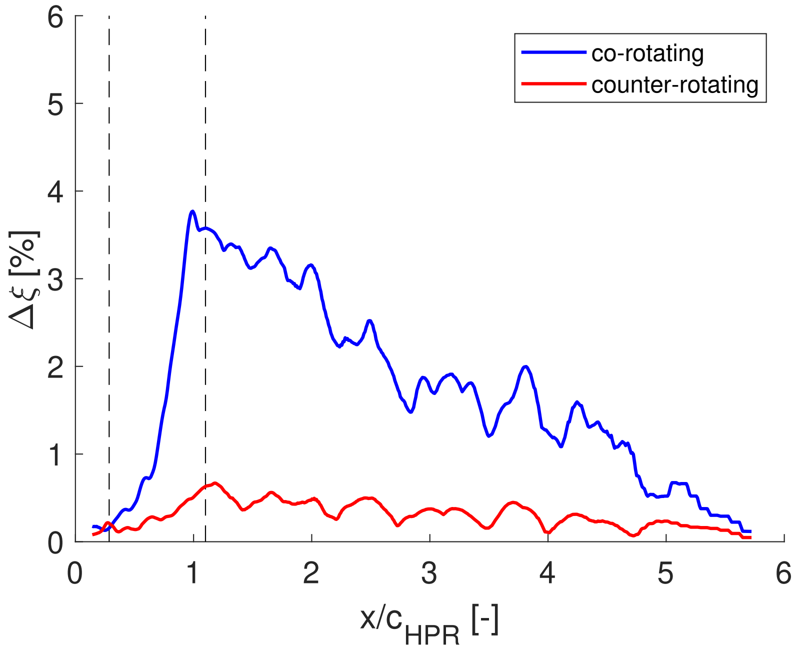

Figure D.2: Configuration 1. Total pressure losses variation within one blade passage in the co-rotating and counter-rotating case.

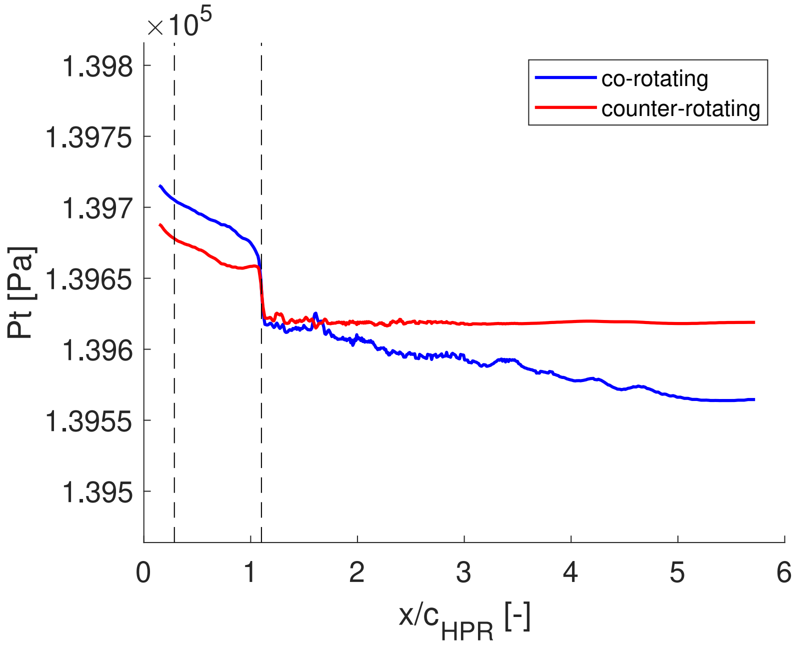

Figure D.3: Configuration 1. Total pressure trend in the co-rotating and counter-rotating case.

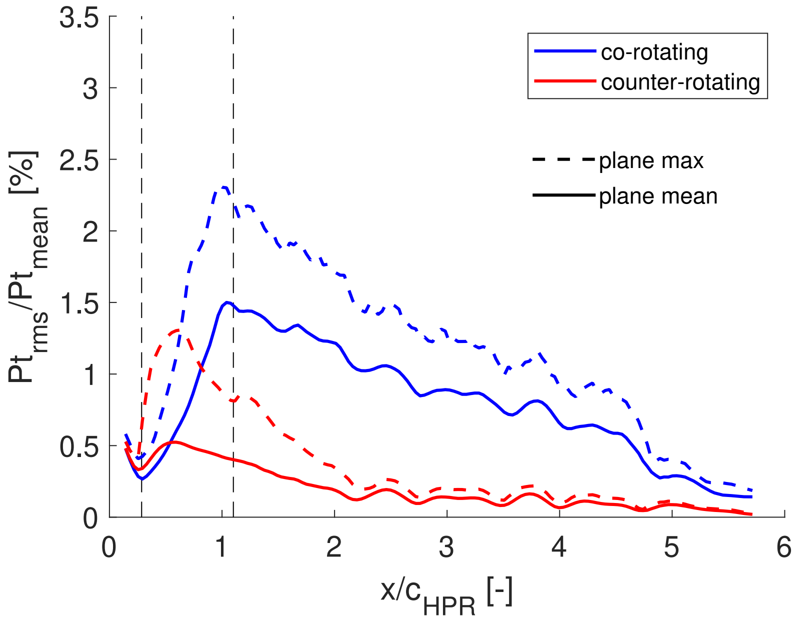

Figure D.4: Configuration 1. Normalized RMS fluctuations of the total pressure in the co-rotating and counter-rotating case. The maximum and mean RMS values for each axial coordinate are normalized with the mean total pressure value.

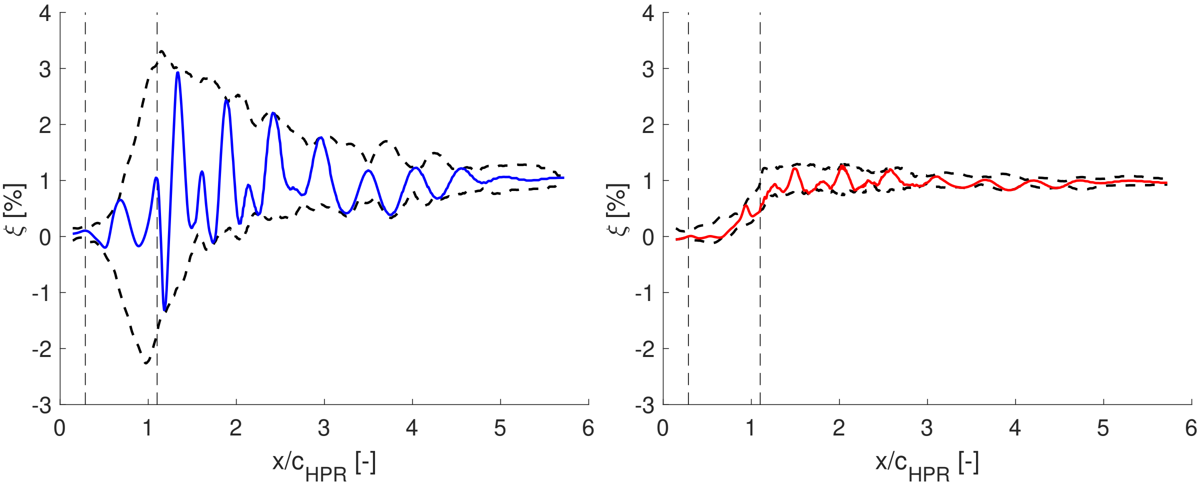

(a) Co-rotating case (b) Counter-rotating case

Figure D.5: Configuration 2. Instantaneous value and envelope of the total pressure losses in the LPV block.

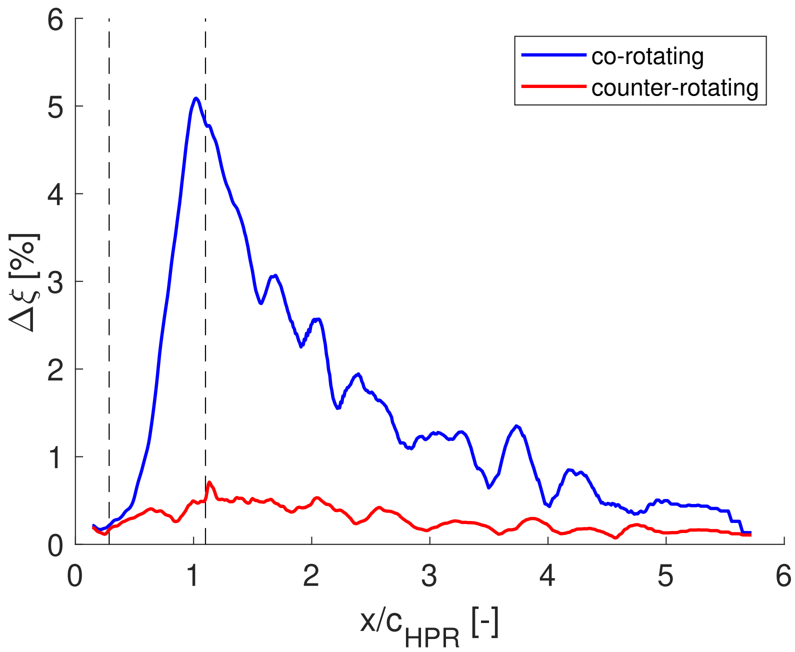

Figure D.6: Configuration 2. Total pressure losses variation within one blade passage in the co-rotating and counter-rotating case.

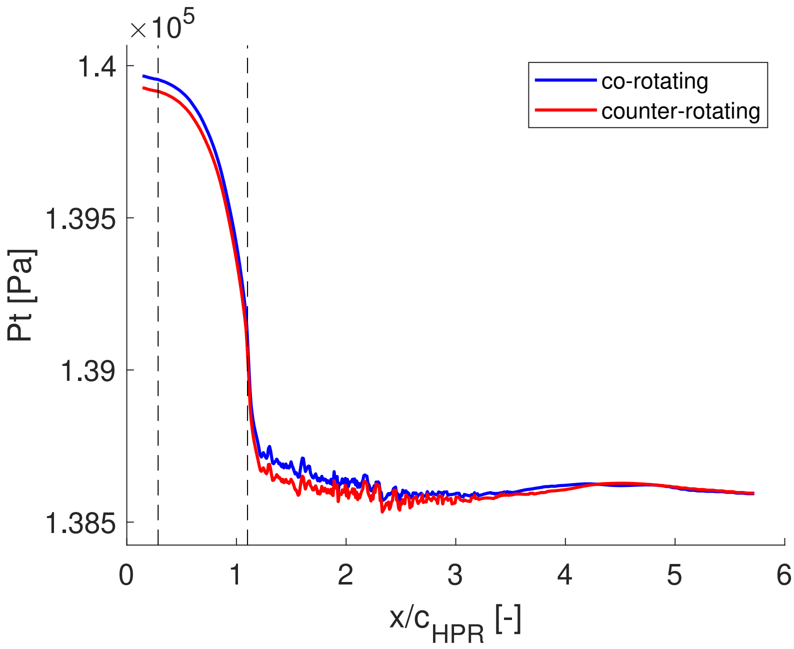

Figure D.7: Configuration 2. Total pressure trend in the co-rotating and counter-rotating case.

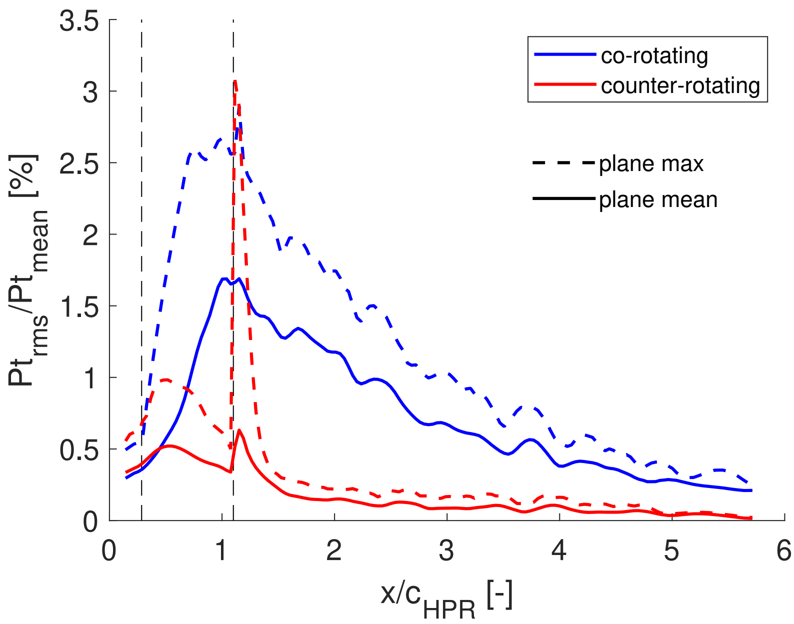

Figure D.8: Configuration 2. Normalized RMS fluctuations of the total pressure in the co-rotating and counter-rotating case. The maximum and mean RMS values for each axial coordinate are normalized with the mean total pressure value.

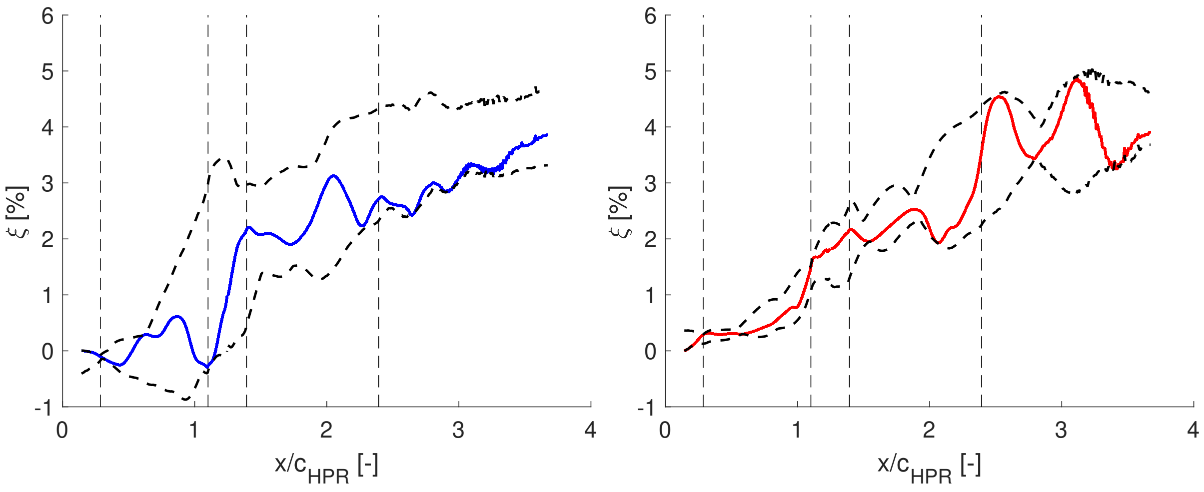

(a) Co-rotating case

(b) Counter-rotating case

Figure D.9: Instantaneous value and envelope of the total pressure losses for the LPV and LPR blocks.

Bibliography

[1] E. Gottlich. «Research on the aerodynamics of intermediate turbine diffusers». In: *Progress in Aerospace Sciences* 47(4) (2011), pp. 249–279 (cit. on p. 1).

[2] A. Firrito, Y. Bousquet, N. Binder, and L. Pintat. «Influence of turbulence boundary conditions on RANS and URANS simulations for an inter-turbine duct». In: *Proceedings of ASME Turbo Expo 2020* (2020) (cit. on p. 2).

[3] J. D. Denton. «Loss Mechanisms in Turbomachines». In: *ASME Journal of Turbomachinery* 115 (1993) (cit. on pp. 2, 23).

[4] D. C. Wisler. «The Technical and Economic Relevance of Understanding Boundary Layer Transition in Turbomachinery». In: Lecture series, von Karman Institute for Fluid Dynamics (1998) (cit. on p. 3).

[5] P. G. Hill, U. W. Schaub, and Y. Senoo. «Turbulent Wakes in Pressure Gradients». In: *Journal of Applied Mechanics* (1963) (cit. on pp. 6, 7).

[6] H. Schlichting. *Boundary Layer Theory*. New York, N. Y.: McGraw-Hill Book Company, Inc., 1960 (cit. on p. 5).

[7] L. H. Smith. «Discussion of ASME Paper No. 96-GT-029: Wake Mixing in Axial Flow Compressors». In: *ASME Turbo Expo* (1996) (cit. on p. 7).

[8] D. E. Van Zante, J. J. Adamczyk, A. J. Strazisar, and T. H. Okiishi. «Wake Recovery Performance Benefit in a High-Speed Axial Compressor». In: *ASME Journal of Turbomachinery* 124 (2002) (cit. on p. 7).

[9] H. P. Hodson and W. N. Dawes. «On the Interpretation of Measured Profile Losses in Unsteady Wake-Turbine Blade Interaction Studies». In: *ASME Journal of Turbomachinery* 120 (1998) (cit. on p. 8).

[10] A. G. van de Wall, J. R. Kadambi, and J. J. Adamczyk. «A Transport Model for the Deterministic Stresses Associated With Turbomachinery Blade Row Interactions». In: *ASME Journal of Turbomachinery* 122 (2000) (cit. on pp. 8, 25, 27, 40, 41).

[11] T. Praisner, J. Clark, T. Nash, M. Rice, and E. Grover. «Performance impacts due to wake mixing in axial-flow turbomachinery». In: *ASME Turbo Expo 2006* (2006) (cit. on pp. 8, 9, 40, 50).

[12] M. G. Rose and N. W. Harvey. «Turbomachinery Wakes: Differential Work and Mixing Loss». In: *ASME Journal of Turbomachinery* 122 (2000), pp. 68–77 (cit. on pp. 9, 10).

[13] M. G. Rose, P. Schupbach, and M. Mansour. «The Thermodynamics of Wake Blade Interaction in Axial Flow Turbines: Combined Experimental and Computational Study». In: *ASME Journal of Turbomachinery* 135.3 (2013) (cit. on pp. 9–11).

[14] M. Marx, M. G. Rose, S. Staudacher, and K. Engel. «Unsteady Work and Wake Recovery due to the Pressure Wave Interaction in a LP Turbine». In: *Proceedings of ASME Turbo Expo 2015* (2015) (cit. on p. 9).

[15] R. Dean. «On the Necessity of Unsteady Flow in Fluid Machines». In: *Journal of Basic Engineering* 81 (1959), pp. 24–28 (cit. on p. 10).

[16] L. H. Smith. «Wake Dispersion in Turbomachines». In: *ASME Journal of Basic Engineering* 88.3 (1966) (cit. on pp. 10, 25).

[17] J. F. Louis. «Axial flow contra-rotating turbines». In: *ASME* (1985) (cit. on p. 11).

[18] P. Rajeevalochanama, S. N. A. Sunkaraa, S. V. R. Murthy, and R. S. Kumaran. «Design of a two spool contra-rotating turbine for a turbo-fan engine». In: *Propulsion and Power Research* 9.3 (2020), pp. 225–239 (cit. on p. 11).

[19] C. Hirsch and M. Aubé. «Numerical Investigation of a 1-1/2 Axial Turbine Stage at Quasi-Steady and Fully Unsteady Conditions». In: *Proceedings of ASME Turbo Expo 2001* (2001) (cit. on pp. 14, 48, 49).

[20] L. Cambier, M. Gazaix, S. Heib, S. Plot, M. Poinot, J.-P. Veuillot, J.-F. Boussuge, and M. Montagnac. «An Overview of the Multi-Purpose elsA Flow Solver». In: *Aerospace Lab journal, ONERA* (2011) (cit. on p. 19).

[21] A. Fourmaux. «Assessment of a low storage technique for multi-stage turbomachinery Navier–Stokes computations». In: *ASME Winter Annual Meeting* (1994) (cit. on p. 20).

[22] A. Jameson and S. Yoon. «Lower-upper implicit schemes with multiple grids for the Euler equations». In: *AIAA Journal* 25.7 (1987), pp. 929–935 (cit. on p. 20).

[23] D. C. Wilcox. «Re-assessment of the scale-determining equation for advanced turbulence models». In: *AIAA Journal* 26.11 (1988), pp. 1299–1310 (cit. on p. 20).

[24] C. Gear. *Numerical Initial Value Problems in Ordinary Differential Equation*. Upper Saddle River, NJ, United States: Prentice-Hall, 1971 (cit. on p. 20).

[25] *FINE Turbo v9.0 User Manual*. NUMECA International. 2013 (cit. on p. 21).

[26] Antares Development Team. «Antares Documentation, Release 1.18.0». In: (2021). URL: `https://www.cerfacs.fr/antares` (cit. on p. 23).